Monthly Notices of the ROYAL ASTRONOMICAL SOCIETY

MNRAS **500,** 5500–5514 (2021) doi:10.1093/mnras/staa3606
Advance Access publication 2020 November 20

A warm molecular ring in AG Car: composing the mass-loss puzzle

C. Bordiu [1,2★] F. Bufano,[1] L. Cerrigone,[3] G. Umana,[1] J. R. Rizzo,[2,4] C. S. Buemi,[1] P. Leto [1] F. Cavallaro [1,5] A. Ingallinera [1] S. Loru,[1] C. Trigilio[1] and S. Riggi[1]

[1]*INAF-Osservatorio Astrofisico di Catania, Via Santa Sofia 78, I-95123 Catania, Italy*
[2]*Centro de Astrobiología (INTA-CSIC), Ctra. M-108, km. 4, Torrejón de Ardoz, E-28850 Madrid, Spain*
[3]*Joint ALMA Observatory, Alonso de Córdova 3107, Vitacura, 7630000, Santiago, Chile*
[4]*ISDEFE, Beatriz de Bobadilla 3, E-28040 Madrid, Spain*
[5]*Department of Astronomy, The Inter-University Institute for Data Intensive Astronomy (IDIA), University of Cape Town, Private Bag X3, Rondebosch, 7701, South Africa*

Accepted 2020 November 13. Received 2020 November 6; in original form 2020 September 8

ABSTRACT

We present APEX observations of CO $J = 3 \rightarrow 2$ and ALMA observations of CO $J = 2 \rightarrow 1$, ^{13}CO $J = 2 \rightarrow 1$, and continuum towards the Galactic luminous blue variable AG Car. These new observations reveal the presence of a ring-like molecular structure surrounding the star. Morphology and kinematics of the gas are consistent with a slowly expanding torus located near the equatorial plane of AG Car. Using non-LTE line modelling, we derived the physical parameters of the gas, which is warm ($\sim$50 K) and moderately dense ($\sim 10^3$ cm^{-3}). The total mass of molecular gas in the ring is 2.7 ± 0.9 M$_\odot$. We analysed the radio continuum map, which depicts a point-like source surrounded by a shallow nebula. From the flux of the point-like source, we derived a current mass-loss rate of $\dot{M} = (1.55 \pm 0.21) \times 10^{-5}$ M$_\odot$ yr^{-1}. Finally, to better understand the complex circumstellar environment of AG Car, we put the newly detected ring in relation to the main nebula of dust and ionized gas. We discuss possible formation scenarios for the ring, namely, the accumulation of interstellar material due to the action of the stellar wind, the remnant of a close binary interaction or merger, and an equatorially enhanced mass-loss episode. If molecular gas formed *in situ* as a result of a mass eruption, it would account for at least a 30 per cent of the total mass ejected by AG Car. This detection adds a new piece to the puzzle of the complex mass-loss history of AG Car, providing new clues about the interplay between LBV stars and their surroundings.

Key words: stars: evolution – stars: individual: AG Carina – stars: massive – stars: mass-loss – ISM: abundances – ISM: molecules.

1 INTRODUCTION

Over the course of their lifetime, massive stars have a great impact in the chemistry, structure, and dynamics of the interstellar medium (ISM). This impact intensifies as they enter the luminous blue variable (LBV) phase, a brief ($\sim 10^4$ yr) and unstable post-main-sequence stage, in which massive stars exhibit the highest mass-loss rates (up to 10^{-3} M$_\odot$ yr^{-1}). Such a copious mass-loss occurs by virtue of dense and steady stellar winds and, sporadically, violent outbursts like the Great Eruption of η Car in the 19th century. The interaction between this mass-loss, interstellar material, and different wind regimes shapes the closest circumstellar environment, leading to the formation of large multiphase nebulae.

Nebulae around LBV stars (LBVNs) therefore emerge as valuable laboratories to understand the feedback mechanisms between the parent stars and their environment. The multiwavelength study of this circumstellar material is a crucial tool to trace back the mass-loss record of these sources throughout their different evolutionary phases (e.g. Umana et al. 2005, 2009, 2010; Agliozzo et al. 2014; Cerrigone et al. 2014; Buemi et al. 2017). However, most of the research so far has focused on the dust and ionized gas content of LBVNs, paying little attention to the missing piece of the picture: the molecular gas.

In recent years, carbon monoxide and a handful of other simple molecular species have been detected in the surroundings of several candidate and confirmed LBVs, such as G79.29+0.46 (Rizzo, Jiménez-Esteban & Ortiz 2008, Rizzo et al. 2014), [GKF2010] MN101 (=MGE 042.0787+00.5084, Bordiu, Rizzo & Ritacco 2019), and the well-known η Car (Smith & Davidson 2001; Loinard et al. 2012; Loinard et al. 2016; Smith; Ginsburg & Bally 2018a; Bordiu & Rizzo 2019; Gull et al. 2020; Morris et al. 2020). All these successful detections demonstrate that, provided the adequate physical conditions, conspicuous amounts of molecular gas can arise and survive for some time in the hostile outskirts of these stars. By analysing the emission at mm- and sub-mm wavelengths from rotational transitions of CO and other species, one can obtain valuable kinematic information that allows for precisely reconstructing previous mass-loss events and place constraints on the time-scales of the observed structures. Therefore, the very existence of these molecules opens a complementary window to learn about the mass-loss phenomena in these hot, massive stars, beyond what is

★ E-mail: cristobal.bordiu@inaf.it

© 2020 The Author(s)
Published by Oxford University Press on behalf of the Royal Astronomical Society

Downloaded from https://academic.oup.com/mnras/article/500/4/5500/5996198 by INAF Trieste (Osservatorio Astronomico di Trieste) user on 20 January 2021

visible at other wavelengths. In addition, the determination of the relative chemical abundances and isotopic ratios in the molecular gas provides valuable snapshots of the stellar chemistry.

Among the scant LBV family, AG Car stands out as one of the most luminous members ($L \sim 1.5 \times 10^6$ $L_\odot$, Groh, Hillier & Damineli 2011). Located in the far side of the Carina arm, the literature establishes a canonical distance of 6 ± 1 kpc (Humphreys et al. 1989). Revisions on this value were recently made by Smith & Stassun (2017) and Smith et al. (2019) based on *Gaia* parallaxes. They concluded that AG Car may be 20 per cent closer, at a distance of $4.7^{+1.2}_{-0.8}$ kpc, which is consistent, within the uncertainties, with the previous estimate. Hereafter in this work, we adopt the canonical distance of 6 kpc.

AG Car has been widely observed across the whole electromagnetic spectrum for decades. The star is surrounded by a slightly bipolar ring nebula of about 30×40 arcsec that was first reported by Thackeray (1950). Further dynamic studies of the nebula in the light of Hα, [N II] and [S II] by Thackeray (1977) concluded that the nebula was a hollow shell with hints of bipolarity, expanding at $\sim$50 km s^{-1}. Humphreys et al. (1989) determined a kinematic age for the nebula of $\sim 10^4$ yr, consistent with the duration of the LBV phase. Broad-band optical continuum observations by Paresce & Nota (1989) revealed a helical jet-like structure in the NE–SW direction, apparently arising from the star, which gave rise to questions about the possible binarity of AG Car. However, no signature of a companion star was detected (Nota et al. 1992). Smith (1991) and Nota et al. (1992) revisited the dynamics of the nebula, establishing an expansion velocity of 70 km s^{-1} and identifying a bipolar outflow at 83 km s^{-1} distorting the NE side of the shell. Later, ATCA observations at 3 and 6 cm by Duncan & White (2002) detected radio continuum emission arising from the star and the shell, with a spectral index consistent with thermal radiation from ionized gas. Finally, the dust content of the nebula was thoroughly investigated by Voors et al. (2000) and Vamvatira-Nakou et al. (2015) (hereafter VN15) by means of infrared imaging and spectroscopy. The latter estimated a total nebular mass of $\sim$15 $M_\odot$ and proposed a mass eruption with a kinematic age of 1.7×10^4 yr as the origin of the structure.

None the less, what makes AG Car particularly interesting is its extreme variability. AG Car exhibits yearly micro-variations of 0.1–0.5 mag superimposed to a more than a decade-long S Dor cycle, with visual changes of $\sim$2 mag between the hot and cool state (Humphreys & Davidson 1994; Stahl et al. 2001; Sterken 2003). For that reason, AG Car is an excellent laboratory to learn about the formation and destruction of molecules in a changing environment, in terms of physical conditions and time-scales.

The first attempts to detect molecular gas associated with AG Car were made by Nota et al. (2002; hereafter N02), targeting the CO $J = 1 \rightarrow 0$ and $J = 2 \rightarrow 1$ lines with the SEST telescope. With a series of single-dish pointings, they coarsely sampled the region around the star, with beam sizes of 45 and 23 arcsec and spacings of 45 and 12 arcsec, respectively. Their spectra displayed multiple narrow velocity components, likely related to intervening sheets of molecular gas, but also a broad component centred at 26 km s^{-1}. The authors interpreted this broad component, which presented a pseudo-Gaussian profile, as arising from a circumstellar expanding envelope or disc, for which they estimated a minimum mass of 2.8 $M_\odot$. Despite this promising result, the region was never properly imaged at higher resolution to confirm the existence of such a structure.

In this work, we report APEX and ALMA observations of CO and ^{13}CO towards AG Car, confirming the detection of a molecular ring surrounding the star. The paper is structured as follows: in Section 2 we summarize the molecular line observations; in Section 3 we describe the main findings; in Section 4 we analyse the morpho-kinematic features of the structure, derive the physical parameters of the gas, and present a kinematic model. In the same section, we also discuss possible formation mechanisms. In Section 5, we put together the available data into a single, unified picture of the mass-loss record of AG Car; and finally, in Section 6 we present the conclusions of this study and lay the groundwork for further research on AG Car.

2 OBSERVATIONS

2.1 APEX observations

We observed AG Car with the Atacama Pathfinder EXperiment (APEX) telescope, located at Llano de Chajnantor (Chile). Observations took place on 2014 September 23 as part of the program E-094.D-0598A (P.I: G. Umana). The front-end used was the APEX2 receiver of the Swedish Heterodyne Facility Instrument (Vassilev et al. 2008), targeting the CO $J = 3 \rightarrow 2$ transition at 345.796 GHz. The eXtended Fast Fourier Transform Spectrometer (Klein et al. 2012) provided an instantaneous bandwidth of 2.5 GHz with 32 768 channels, resulting in an effective velocity resolution of about 0.07 km s^{-1} at the observing frequency.

An On-The-Fly map of 100×100 arcsec around the source was done in Total Power mode, using the off position $\alpha = 10^{\rm h}49^{\rm m}23\overset{\rm s}{.}3$, $\delta = -60^\circ 58' 47\overset{''}{.}7$ (J2000). At the rest frequency of the line, the APEX primary beam is 19.2 arcsec. Observations were performed under average weather conditions (1–2 mm of precipitable water vapour). Calibration was done using Mars and X TrA, and pointing and focus were checked regularly during the night.

The raw spectra produced by the APEX standard pipeline was reduced using the GILDAS[1] software package. This process involved the removal of bad scans, a linear baseline fitting and a velocity smoothing to a final resolution of 1 km s^{-1} to improve rms. Conversion from the original antenna temperatures (T_A^*) to main-beam brightness temperature ($T_{\rm mb}$) was done by correcting for the forward-hemisphere efficiency and the beam efficiency of the antenna, so that

$$T_{\rm mb} = T_{\rm A}^* \frac{F_{\rm eff}}{B_{\rm eff}}. \quad (1)$$

For the APEX telescope, $F_{\rm eff} = 0.97$ and $B_{\rm eff} = 0.73$ at 345 GHz. The typical rms noise per 1 km s^{-1} channel in the final cube is 50 mK.

2.2 ALMA observations

Follow-up observations of AG Car were conducted on 2019 October 2 and 6, with the ALMA 7-m and total power arrays, respectively, in the context of the program 2019.1.01056.S (P.I: L. Cerrigone). It was mapped the spatial distribution of the rotational $J = 2 \rightarrow 1$ transitions of CO and ^{13}CO at 1.3 mm. The source was observed with three total-power antennas under excellent weather conditions (pwv $\sim$ 0.25 mm) and with 10 7-m antennas under good conditions (pwv $\sim$ 1.25 mm).

The spectral set-up consisted of two spectral windows centred at 220.398 and 230.538 GHz plus two additional windows for continuum. The correlator was tuned to provide an instantaneous bandwidth of 1850 MHz in 2048 channels, with a moderate velocity resolution of about 1.3 km s^{-1} for each line.

[1] http://www.iram.fr/IRAMFR/GILDAS

Downloaded from https://academic.oup.com/mnras/article/500/4/5500/5996198 by INAF Trieste (Osservatorio Astronomico di Trieste) user on 20 January 2021

Table 1. Observational parameters.

Line	ν_0 (GHz)	Telescope	θ (arcsec)
CO $J = 2 \rightarrow 1$	230.538	ACA	7.0×5.2
		TP	28.2
^{13}CO $J = 2 \rightarrow 1$	220.398	ACA	7.2×6.0
		TP	29.5
CO $J = 3 \rightarrow 2$	345.795	APEX	19.2

ACA data were calibrated with CASA v.5.6.1-8 and the ALMA pipeline version 42 686 that comes with it. Calibrators J1047-6217 and J1058+0133 were used for bandpass and flux calibration. Cubes of line emission, with a characteristic beam of 7 × 5 arcsec, were constructed from the calibrated visibilities using the CLEAN algorithm after continuum-subtraction. CASA v5.6.1-8 and pipeline v.42686 were also used for the reduction of the single-dish data. The observations were performed in position-switching mode, with an off position chosen by the ALMA Observatory among known clean areas for Galactic sources. The off position was about 4° away from our target. Such a large angular distance between the target and the off position caused ripples in the spectra, which we did not attempt to remove in post-processing, since their amplitude is negligible with respect to the brightness of the spectral lines from our target. The flux calibration was based on Kelvin-to-Jansky factors estimated from calibration campaigns performed by the Observatory. At our frequencies the factors had a value of about 41.5 K Jy^{-1}.

Finally, to recover all the spatial scales and avoid missing flux, we combined the ACA and the Total Power (hereafter ALMA TP) cubes with the CASA `feather` task, which involved regridding the single-dish data and correcting it for the primary beam response. The feathered cubes recover 99.7 per cent of the single-dish flux.

The resulting products were then re-scaled from flux densities to brightness temperature using the standard equation:

$$T_{\rm mb} = 1.222 \times 10^6 \frac{S_\nu}{\nu^2 \theta_{\rm maj} \theta_{\rm min}}, \quad (2)$$

where S_ν denotes the flux density in Jy beam^{-1}, ν is the reference frequency in GHz, and $\theta_{\rm maj}$ and $\theta_{\rm min}$ are the major and minor axes of the beam in arcsec, respectively. The typical rms noise level per channel of 1.3 km s^{-1} ranges from 5 to 10 mK. Similarly, the rms noise level of the continuum map is ∼1.2 mJy beam^{-1}.

A summary of the observing parameters is presented in Table 1. Throughout this paper, we use the following conventions: (1) intensities of emission lines are expressed in $T_{\rm mb}$ scale; (2) intensities of continuum are expressed in flux density scale; (3) velocities refer to the local standard of rest frame (LSR); and (4) positions are offsets from the coordinates of AG Car, $\alpha = 10^{\rm h}56^{\rm m}11\overset{\rm s}{.}5779$, $\delta = -60°27'12\overset{''}{.}8095$ (J2000; Gaia Collaboration 2016).

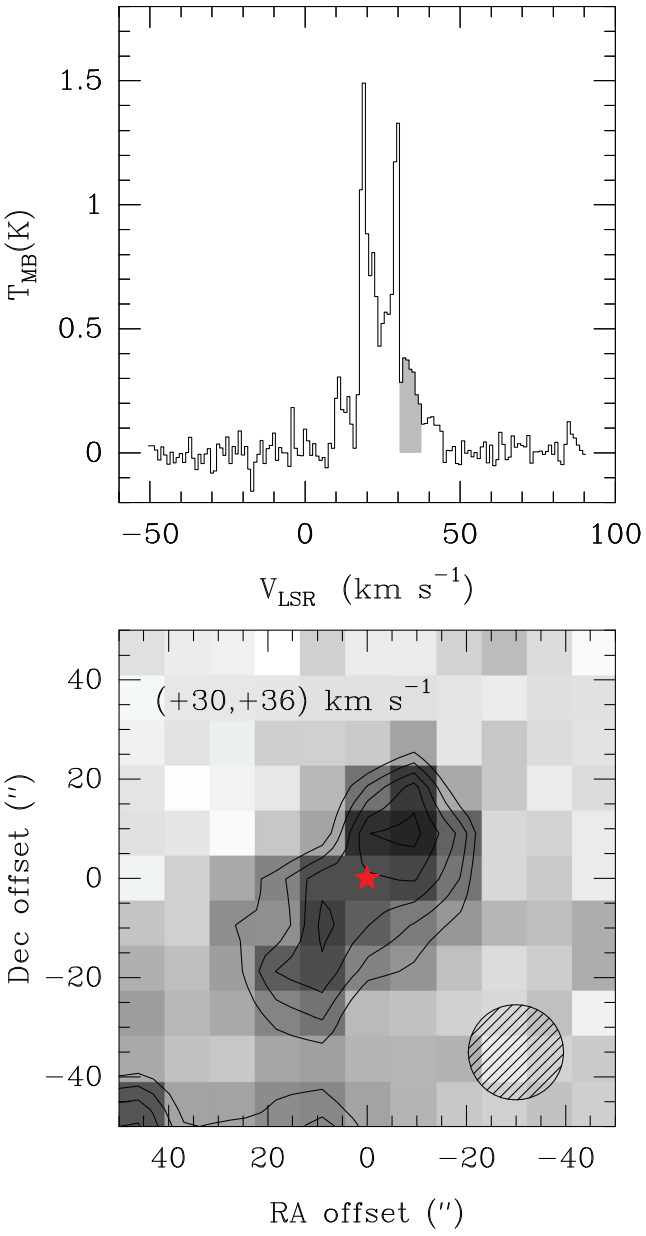


Figure 1. APEX CO $J = 3 \rightarrow 2$ emission towards AG Car. Top panel: spectrum averaged in the 100 × 100 arcsec field. The velocity range integrated in the bottom panel is filled in grey. Bottom panel: velocity-integrated intensity map from 30 to 36 km s^{-1}, corresponding to the filled area in the top panel. Contours start at 2.5 K km s^{-1} in steps of 0.5 K km s^{-1}. The red marker indicates the position of the star, and the hatched circle in the bottom right corner represents the APEX primary beam size.

3 RESULTS

3.1 APEX sigle-dish data

Fig. 1 shows the averaged APEX CO $J = 3 \rightarrow 2$ spectra in the field of AG Car. Most of the emission arises in the velocity range (0, 50) km s^{-1}. We identify multiple velocity components within this range, coincident with the ones reported by N02 in the CO $J = 1 \rightarrow 0$ and CO $J = 2 \rightarrow 1$ transitions: two narrow, dominant components at 18.5 and 29.7 km s^{-1} plus additional minor components at 11, 18.5, 21.5, and 29.5 km s^{-1}. N02 attributed these components to background or foreground contamination from ambient gas moving perpendicularly to the line of sight. We also detect a broad component at 26.5 km s^{-1}, the same one that N02 tentatively associated with the star.

Careful inspection of the spatial distribution of each component shows that all the narrow lines are clumpy and somewhat extended, mainly arising from the southeast and the west. The same applies to the broad component, which is particularly intense towards the centre and the south of the map. However, we note that the 29.5 km s^{-1} narrow line presents a 'shoulder-like' feature consistent with a partially overlapping line at a slightly higher velocity. This component was indeed marginally detected in N02's spectra, without

Downloaded from https://academic.oup.com/mnras/article/500/4/5500/5996198 by INAF Trieste (Osservatorio Astronomico di Trieste) user on 20 January 2021

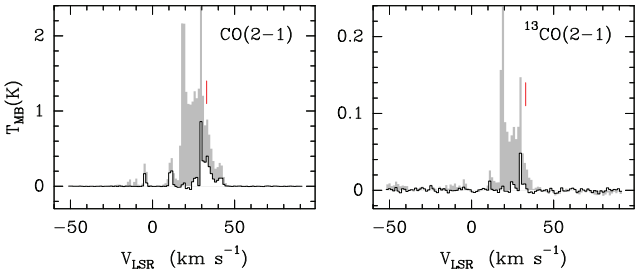


Figure 2. Interferometric filtering towards AG Car. Left-hand panel: CO $J = 2 \rightarrow 1$. Right-hand panel: ^{13}CO $J = 2 \rightarrow 1$. In each panel, feathered ACA+TP (filled) and ACA only spectra (black), averaged within a radius of 20 arcsec from the star, are displayed in the same temperature scale. The red lines indicate the central velocity of the component likely associated with the star.

clear hints of any particular spatial distribution, probably being just a high-velocity wing of the broad component at 26.5 km s^{-1}.

This newly identified component, centred at 32.5 km s^{-1}, has a velocity extension of about 6 km s^{-1} and is significantly weaker than the others. We attempted to isolate the line by removing the neighbouring components through a Gaussian fitting, but this resulted in the introduction of multiple artefacts that altered the line shape. None the less, integration of the approximate velocity range of the line, i.e. at least 30–36 km s^{-1}, represented in grey in the figure, reveals the existence of an elongated structure towards the centre of the field (Fig. 1, bottom panel). Despite being possibly contaminated by the adjacent narrow component, the structure exhibits a certain degree of bipolar symmetry with respect to AG Car, with two 'lobes' along the SE–NW axis. None of the other ambient components show a comparable spatial distribution.

3.2 ACA interferometric data

3.2.1 CO and ^{13}CO emission

The feathered CO $J = 2 \rightarrow 1$ and ^{13} CO $J = 2 \rightarrow 1$ spectra show essentially the same features visible in the CO $J = 3 \rightarrow 2$ APEX data. Fig. 2 compares the feathered (filled) and the ACA-only (black) spectra for the two observed lines. The interferometer filtered out most of the emission at $v_{LSR} < 30$ km s^{-1}, including the broad line at 26.5 km s^{-1}. Considering the ACA maximum recoverable scale is 28 arcsec at 230 GHz (our shortest baseline was ∼8.9 m), these components necessarily correspond to extended, large-scale emission, as previously discussed. On the other hand, a significant fraction of the flux in the velocity range (+ 30, +40) km s^{-1} is preserved, suggesting that this emission is considerably more compact than the ambient material. From the peak temperature, we estimate that ACA recovers ∼50 per cent of the single-dish flux in this range.

Fig. 3 shows the integrated intensity map of the CO $J = 2 \rightarrow 1$ line in the range (+29, +36 km s^{-1}). ACA's synthesized beam (of ∼7 arcsec) improves angular resolution with respect to APEX by a factor of ∼3. Such improvement allows us to resolve the emission, revealing an elliptical structure enclosing AG Car and apparently detached from the star. Two remarkably symmetric 'lobes' dominate the emission, south-east and north-west of the star, peaking at (10 arcsec, –10 arcsec) and (–10 arcsec, 10 arcsec), respectively. The lobes appear connected by two fainter arcs. A large clump at position (–25 arcsec, –5 arcsec) disrupts the structure in its westernmost side. This clump is related to residuals from the narrow component at

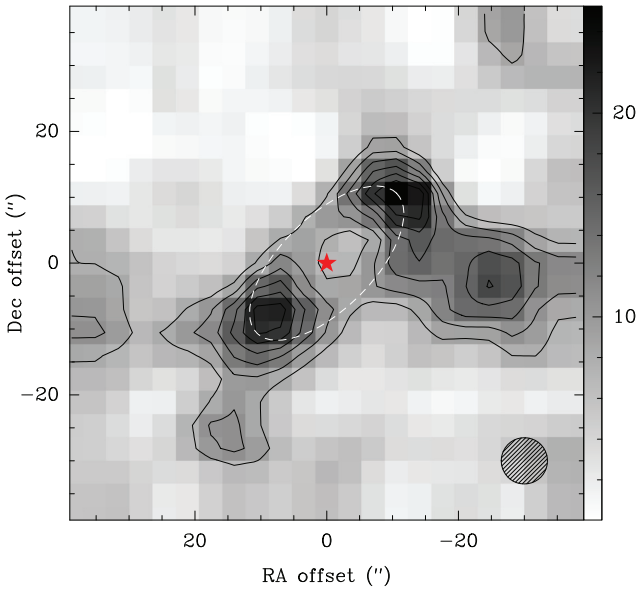


Figure 3. ACA+TP velocity-integrated intensity map of CO $J = 2 \rightarrow 1$ towards AG Car, in the velocity range (+29, +36) km s^{-1}. Contours start at 8 K km s^{-1} in steps of 2.5 K km s^{-1}. The red marker indicates the position of the star, and the hatched circle in the bottom right corner represents the ACA synthesized beam size. The dashed ellipse represents the ellipse used for the fitting.

29.5 km s^{-1} that are visible in the ACA spectra (perhaps the densest part of an extended cloud). The S/N ratio across the ring ranges from 6σ to 14σ, which means that even the faintest parts are genuine. By fitting an ellipse to the lobes, we derive an approximate angular size of 35 × 15 arcsec, with a position angle of 135° east of north. The orientation and size of the ellipse match perfectly the NW–SE elongation of the infrared shell reported by Voors et al. (2000) from continuum and [Ne II] imagery. In the ^{13}CO $J = 2 \rightarrow 1$ integrated intensity map (not shown), only the lobes of the structure are visible, with an S/N ratio slightly above 5σ. The non-detection of fainter arcs is likely due to the limited sensitivity.

3.2.2 Radio continuum emission

Radio continuum emission traces the ionized gas in the nebula of AG Car. Fig. 4 shows the ACA radio continuum map of AG Car at 225 GHz. Emission is dominated by an unresolved compact source in the centre of the field, presumably related to the star. Weak emission arising from the brightest parts of the optical nebula are visible as well above the 3σ level.

The radio morphology is slightly different from the 5.5 and 8.8 GHz ATCA maps presented by Duncan & White (2002), which depict a compact source surrounded by a bright and very clumpy detached nebula. Note, though, that ATCA data has a higher spatial resolution (1 arcsec at 8.5 GHz) and provides a more complete *uv* coverage.

We fitted a 2D Gaussian to the compact source, measuring a flux density of 30.2 ± 2.2 mJy. The uncertainty is the quadratic sum of the rms noise in the map and a calibration error of 5 per cent. The resulting value does not match the expected flux density obtained by extrapolating the spectral index $\alpha = -0.1$ reported by Duncan & White 2002, which is 0.89 mJy. Such discrepancy implies that either the spectral index is variable, and thus the current physical conditions in the star are quite different from those in the 1994–1996

Downloaded from https://academic.oup.com/mnras/article/500/4/5500/5996198 by INAF Trieste (Osservatorio Astronomico di Trieste) user on 20 January 2021

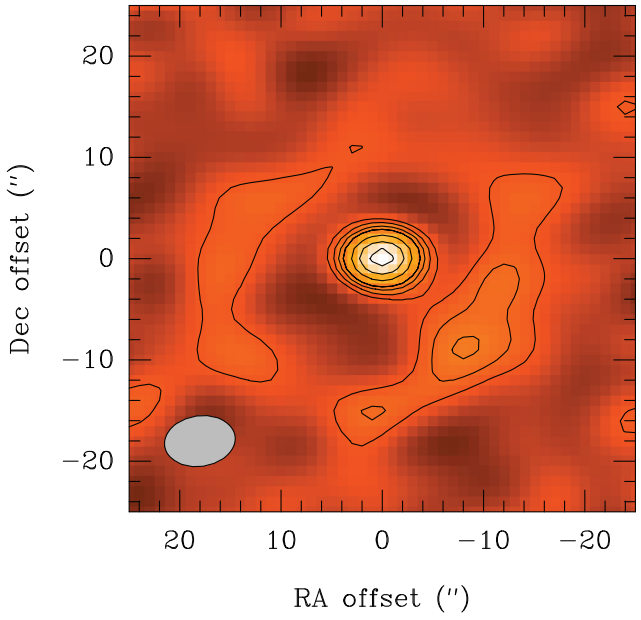


Figure 4. ACA 225 GHz radio continuum map of AG Car. Contours start at 2.5 mJy, with steps of 2.5 mJy. The synthesized beam is shown in the bottom left corner.

period (when the ATCA data were gathered), or that another emitting component is superposed at mm-wavelengths, such as thermal dust close to the star, effectively pushing the spectral index towards more positive values. Finally, if we ignore the 25-yr gap between the observations and combine the fluxes, we obtain a spectral index $\alpha \sim 0.8$, compatible with a typical stellar wind.

We determined a nebular flux of 40 ± 15 mJy after subtracting the contribution of the point source. Again, this value does not match the extrapolation of the −0.1 spectral index reported by Duncan & White (2002), which yields a slightly higher flux. We note, though, that the LAS (largest angular scale) of ACA at 225 GHz is about one third of the LAS of ATCA 750B configuration at 5.5 GHz, so it is very likely that we are missing a fraction of the extended flux.

4 LINKING THE MOLECULAR RING TO AG CAR

4.1 Morphology and kinematics

To establish a physical connection between the CO structure and AG Car, we need to analyse the morphology and kinematics of the gas and put them in context with the surrounding ISM. AG Car lies in projection amid the massive star clusters Tr 14 and Tr 16 and the large Car OB2 association. Towards these structures, i.e. from $l = 287°$–$290°$, several giant molecular clouds are observed. Most of them arise at negative systemic velocities, comprised between −10 and $-30\,\mathrm{km\,s^{-1}}$, corresponding to distances of 2–3 kpc on the near side of the Carina arm (Cohen et al. 1985). These clouds are dense, clumpy, and continuously eroded by intense UV radiation from hundreds of newborn OB stars (e.g. Rizzo & Arnal 1998; Rathborne et al. 2002; Wu et al. 2018). On the contrary, the emission in the field of AG Car appears at $v_{\rm LSR} > 10\,\mathrm{km\,s^{-1}}$. In this direction, these positive velocities are expected for gas on the far side of Carina (Grabelsky et al. 1987), which agrees with the distance of 6 kpc assumed for the star.

A closer look at the distribution of the emission in the field of AG Car highlights the differences between the central CO structure and the other velocity components. Fig. 6 shows the APEX CO $J = 3 \rightarrow 2$ velocity-integrated intensity maps of the dominant lines, i.e. the two narrow lines at 18.6 and $29.6\,\mathrm{km\,s^{-1}}$ and the broad component at $26.5\,\mathrm{km\,s^{-1}}$ that N02 tentatively linked with the star (labelled C1, C2, and C3 in order of increasing velocity). As mentioned earlier in Section 3.1, none of the three components seem to be morphologically associated with the star, unlike the component around $32.5\,\mathrm{km\,s^{-1}}$ (hereafter C4), shown again for reference. The 'arm' seen in component C3, extending over the source to the East, is due to contamination by the low-velocity wing of component C4 (the two lines overlap significantly).

Most of the emission from C1, C2, and C3 is resolved out by the interferometer, preserving the small-scale features of component C4. As seen in the ACA map, the spatial distribution of C4 is consistent with a circumstellar ring or torus seen at a certain inclination angle. Assuming that such structure is perfectly axisymmetric, we can make an elliptical fit and use the axial ratio $R_{\rm ab}$ to estimate the viewing angle, such that $\theta_i = \arctan(R_{\rm ab})$. This method yields an angle of $\theta_i = 68 \pm 3°$, which implies that the ring is viewed nearly edge-on, with its semimajor axis following the direction in which the infrared shell is slightly elongated (Voors et al. 2000). The deprojected characteristic radius of the structure is thus 15 arcsec, which is equivalent to ∼0.4 pc at a distance of 6 kpc. This physical size is in good agreement with the inner radius of the infrared dusty shell derived by VN15.

The ring extends from 29 to $36\,\mathrm{km\,s^{-1}}$, with a central velocity of $32.5\,\mathrm{km\,s^{-1}}$. In the literature, it is possible to find estimates for the radial velocity of AG Car spanning from 0 to $10\,\mathrm{km\,s^{-1}}$ (e.g. Wolf & Stahl 1982; Humphreys et al. 1989; Stahl et al. 2001; Groh et al. 2009a). Such discrepancy is the consequence of the inherent uncertainty in determining systemic velocities for LBV stars, whose variable stellar winds and circumstellar envelopes often contaminate spectroscopic measurements. Contrarily, the velocity of the CO structure does not depend on any stellar properties. Therefore, in our analysis, we consider a systemic velocity of $32.5\,\mathrm{km\,s^{-1}}$. This velocity is compatible with the distance assuming small departures from Galactic rotation.

Fig. 5 shows the channel maps of the CO $J = 2 \rightarrow 1$ emission in the velocity range of interest. We note that the moderate velocity resolution of our data, of just $1.3\,\mathrm{km\,s^{-1}}$, does not allow us to perform a detailed analysis of the observed kinematic structure, which is sampled by only seven channels. The first two channels, corresponding to $v_{\rm LSR} = 28.2$ and $29.5\,\mathrm{km\,s^{-1}}$, appear highly contaminated, with a prominent clump towards the west particularly bright in the latter. As discussed in Section 3.2, this clump is likely associated with the narrow component at $29.5\,\mathrm{km\,s^{-1}}$: the map of C3 presents relative maximum near position (–25 arcsec, –5 arcsec), as seen in Fig. 6. The rest of the channels are mostly devoid from contamination, except for small faint clumps towards the south. Overall, the emission moves clockwise around the star, from the south-west to the north-west, as velocity increases. The lobes are present across all the channels, with the south-east one being slightly more prominent in the blueshifted channels and vice versa. Contrarily, the arcs that connect the lobes are only visible in the central channels: opening towards the north-east at 29.5 and $30.8\,\mathrm{km\,s^{-1}}$, and towards the south-west at 33.3 and $34.6\,\mathrm{km\,s^{-1}}$.

The velocity gradients observed along the minor and major axes of the structure are mainly compatible with gas moving radially. Two physical scenarios are possible: (1) an accretion disc of gas falling on to the star; or (2) an expanding ring, composed of stellar ejecta or compressed interstellar gas. From an evolutionary perspective,

Downloaded from https://academic.oup.com/mnras/article/500/4/5500/5996198 by INAF Trieste (Osservatorio Astronomico di Trieste) user on 20 January 2021

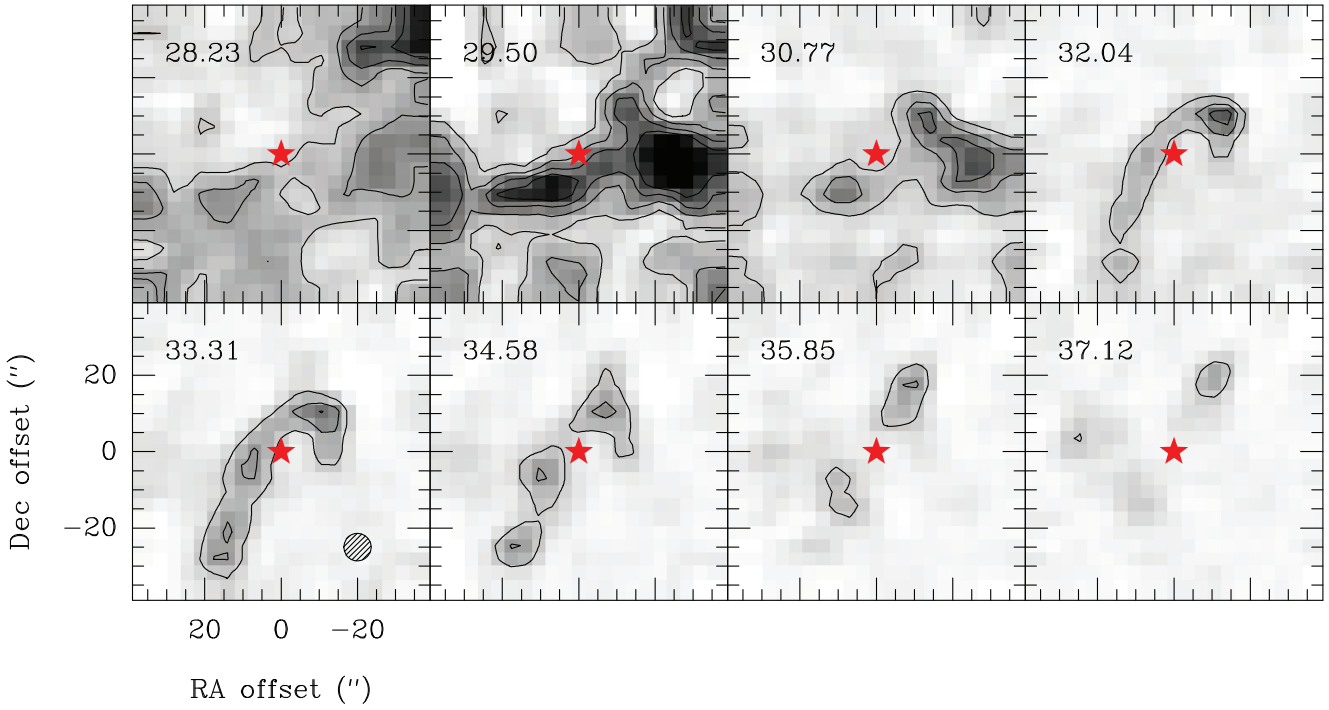


Figure 5. Chanel maps of CO $J = 2 \rightarrow 1$ (ACA+TP). The velocity in km s^{-1} is indicated in the top left corner of each panel. Contours start at $\sim 3\sigma$ in steps of 3σ. The red marker indicates the position of the star, and the hatched circle in the in the bottom left-hand panel represents the approximate ACA synthesized beam.

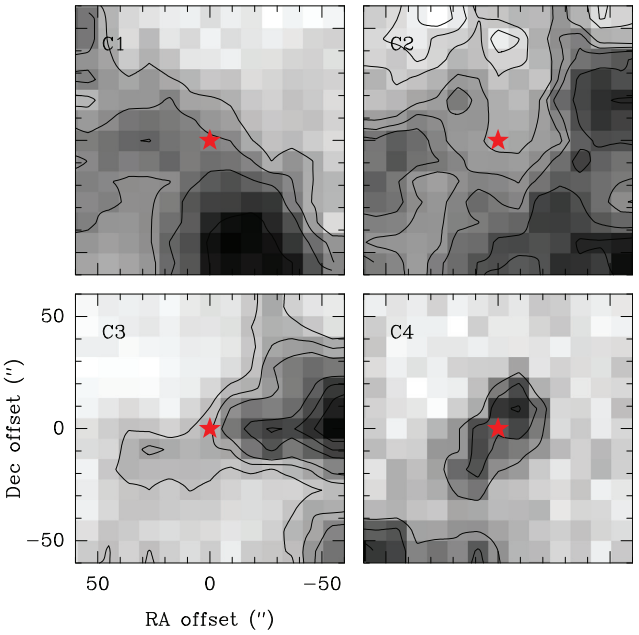


Figure 6. Spatial distribution of the main components in the field of AG Car. APEX CO $J = 3 \rightarrow 2$ velocity-integrated intensity maps of components C1 (from 17.5 to 19.7 km s^{-1}), C2 (from 19.3 to 28.2 km s^{-1}), C3 (from 28.4 to 30.8 km s^{-1}), and C4 (from 30 to 36 km s^{-1}, same as Fig. 1). The colour scale is relative to the peak intensity of each map. Contours at 2.5, 3.5, 4.5, 5.5, 6.5, 8.5, 10.5, and 12.5 K km s^{-1}. The red marker indicates the position of the star.

the accretion disc scenario is highly improbable. Infalling discs around massive stars are expected only in pre-MS stages, and the evolved status of AG Car is more than confirmed. On the other hand, an expanding ring is a much more plausible hypothesis. In this case, the orientation is constrained by the observed velocity gradient: the southeastern part, blueshifted, is the approaching near side, and the northwestern part, redshifted, is then the receding far side. Correcting for the inclination, we estimate an expansion velocity of $v_{\rm exp} = 3.5 \pm 0.5$ km s^{-1}. This value is surprisingly low, considering that typical velocities of LBV winds range from 50 to 100 km s^{-1}. For a characteristic radius of 0.4 pc, the kinematic age of the ring would be $\sim 10^5$ yr. This age must be seen as a strict upper limit, since the structure may be slowing down due to the interaction with the surrounding medium. Yet, the resemblance to the CO torus found in MN101 is noteworthy, having comparable sizes, expansion velocities, and dynamic time-scales (Bordiu et al. 2019). These slow structures could well be the ageing relatives of the 200-yr-old, disrupted molecular torus in η Car (Smith et al. 2018a), which is more compact ($\sim$4000 au) and chemically rich (Bordiu et al. 2019; Gull et al. 2020). The idea of a common formation mechanism for these rings is worth to be studied in more detail. We explore the possible origins of the CO ring in Section 4.3.

4.2 Physical parameters of the gas

If the gas arises from the star – i.e. formed from wind or ejecta – its physical parameters should reflect substantial differences with respect to the ISM. Line ratios are useful diagnostic tools to roughly estimate these parameters. We have three available lines to work with: two transitions of CO plus an additional line of ^{13}CO. However, the analysis is restricted to the single-dish data, i.e. APEX and ALMA TP, since we lack interferometric CO $J = 3 \rightarrow 2$ observations. Thus, we can only provide average values for the structure.

We first computed beam-averaged spectra for the three transitions, centred in the stellar position. Then, we smoothed the resulting averaged spectra to a common velocity resolution of 1.3 km s^{-1}, and we attempted a Gaussian fitting on components C1...C4 with CLASS, as shown in Fig. 7. The results of the fitting are compiled in Table 2. In

Downloaded from https://academic.oup.com/mnras/article/500/4/5500/5996198 by INAF Trieste (Osservatorio Astronomico di Trieste) user on 20 January 2021

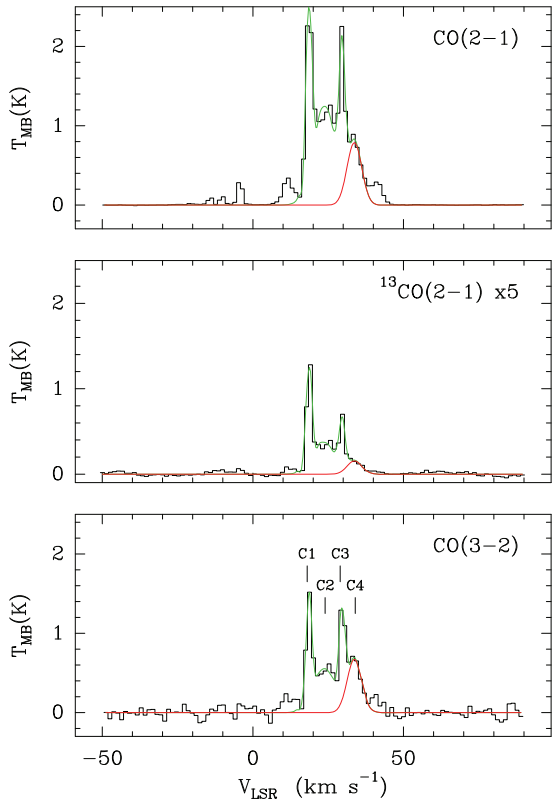


Figure 7. Fitting of the four dominant velocity components in the single-dish spectra. From top to bottom, CO $J = 2 \rightarrow 1$, ^{13}CO $J = 2 \rightarrow 1$ (scaled by a factor of 5) and CO $J = 3 \rightarrow 2$. The green line indicates the sum of the Gaussian fittings of the four components, and the red line highlights the fitting for component C4. The components are labelled in the bottom panel for reference.

some cases, the fitting was rather problematic due to significant line blending, derived from the limited velocity resolution. Therefore, we imposed the condition that every velocity component C_i should have a same full width at half-maximum (FWHM) in each of the three lines, so that the derived line ratios were consistent.

To calculate the line ratios, we used the line intensities integrated over the FWHM of each component, formally expressed as $W = \int T_{\rm mb} {\rm d}v$. The intrinsic uncertainty associated with this magnitude,σ_W, is given by

$$\sigma_W = {\rm rms} \times {\rm d}v \times \sqrt{N}, \quad (3)$$

where rms is the spectrum noise as measured in line-free channels, dv is the velocity resolution, and N is the number of channels (e.g. Mangum & Shirley 2015). Then, we computed the total uncertainty as the quadratic sum of the intrinsic uncertainty plus the calibration uncertainty, so that $\sigma_{\rm tot} = \sqrt{\sigma_W^2 + \sigma_{\rm cal}^2}$. The calibration uncertainties considered are 14 per cent for APEX (APEX2, Dumke & Mac-Auliffe 2010) and 5 per cent for ALMA (Bonato et al. 2018).

Beam dilution becomes a critical issue, as we work with mean values from single-dish data gathered at different frequencies with different instruments. To compute physically meaningful line ratios, we need to apply a beam-filling factor F to the integrated line intensities. We adopt very conservative estimates of $F \leq 0.2$ and $F \leq 0.38$ at 230.538 and 345.799 GHz, respectively, assuming an emitting area comparable to the ACA beam or smaller.

Hereafter, we refer to the CO $J = 3 \rightarrow 2$ to CO $J = 2 \rightarrow 1$ line ratio as R_{32} and to the CO $J = 2 \rightarrow 1$ to ^{13}CO $J = 2 \rightarrow 1$ as $R_{12/13}$. In the ring (component C4) we measure a $R_{32} = 0.45 \pm 0.07$. This value is somewhat low, indicating that the upper level is less populated. On the other hand, we measure a $R_{12/13}$ of 25 ± 4 in C4. This value lies halfway between typical ISM values (Wilson & Matteucci 1992) and those measured in the outskirts of some evolved massive stars, which show nebular ^{12}C/^{13}C ratios as low as 1–5 (Loinard et al. 2012; Bordiu et al. 2019; Rizzo 2019), in agreement with theoretical predictions for extremely processed CNO material (Meynet, Ekström & Maeder 2006). But surprisingly, we measure even lower values in the other velocity components.

To model the excitation of the CO and ^{13}CO lines, we employed the non-LTE radiative transfer code RADEX (van der Tak et al. 2007). RADEX solves the statistical equilibrium equations using the escape probability formulation (Sobolev 1960) to predict the line intensities and level populations. The code presents two important peculiarities. First, it is entirely agnostic to the source geometry, and hence the predicted line intensities need to be corrected for beam dilution. And secondly, it works under the assumption of a homogeneous medium, meaning that all transitions sample the same gas volume with the same excitation conditions. These are obvious oversimplifications, yet extremely convenient to provide first-order estimates, especially considering the nature of our data.

We created a grid of models parametrized by the kinetic temperature $T_{\rm k}$, the CO column density N(CO) and the H_2 volume density $n(H_2)$. The grid covered $T_{\rm k}$ from 10 to 200 K, N(CO) from 10^{13} to 10^{19} cm^{-2}, and $n(H_2)$ from 10^2 to 10^5 cm^{-3}. We used H_2 as the only collision partner, with a cosmic background temperature of 2.73 K. We also adopted a representative FWHM of 6 km s^{-1}.

First, for each $T_{\rm k}$ we used R_{32} and $W_{\rm CO(2-1)}$ to constrain the regions of the parameter space that result in physically meaningful solutions. Sample plots of the fitting are shown in Fig. 8. We find that N(CO) is well determined, being relatively insensitive to temperature and density and taking values of a few 10^{16} cm^{-2}. On the other hand, $n(H_2)$ is only loosely constrained, with valid solutions in the range 10^3–10^4 cm^{-3}. Regarding the temperature, though solutions for $T_{\rm k} >$ 120 K are unlikely, the required volume densities are comparable to those of diffuse clouds ($\sim$100 cm^{-3}), falling well below the critical density of the $J = 2 \rightarrow 1$ transition. Thus, we favour solutions with $T_{\rm k} < 100$ K.

Table 2. Line fitting parameters for each transition: systemic velocity, FWHM, peak temperature, velocity-integrated line intensity, and its error. Values have NOT been corrected for the filling factor.

	CO $J = 2 \rightarrow 1$				^{13}CO $J = 2 \rightarrow 1$				CO $J = 3 \rightarrow 2$			
	$v_{\rm LSR}$ (km s^{-1})	FWHM (km s^{-1})	$T_{\rm peak}$ (K)	W (σW) (K km s^{-1})	$v_{\rm LSR}$ (km s^{-1})	FWHM (km s^{-1})	$T_{\rm peak}$ (K)	W (σW) (K km s^{-1})	$v_{\rm LSR}$ (km s^{-1})	FWHM (km s^{-1})	$T_{\rm peak}$ (K)	W (σW) (K km s^{-1})
C1	18.7	2.2	2.19	5.01 (0.25)	18.6	2.2	0.24	0.54 (0.03)	18.6	2.2	1.31	3.00 (0.44)
C2	23.8	8.9	1.25	11.9 (0.59)	23.5	8.9	0.08	0.71 (0.04)	23.7	8.9	0.56	5.27 (0.79)
C3	29.6	2.3	1.57	3.78 (0.19)	29.6	2.3	0.11	0.26 (0.02)	29.6	2.3	1.05	2.53 (0.38)
C4	33.7	5.7	0.79	4.79 (0.24)	33.7	5.7	0.03	0.19 (0.03)	33.7	5.7	0.67	4.09 (0.62)

Downloaded from https://academic.oup.com/mnras/article/500/4/5500/5996198 by INAF Trieste (Osservatorio Astronomico di Trieste) user on 20 January 2021

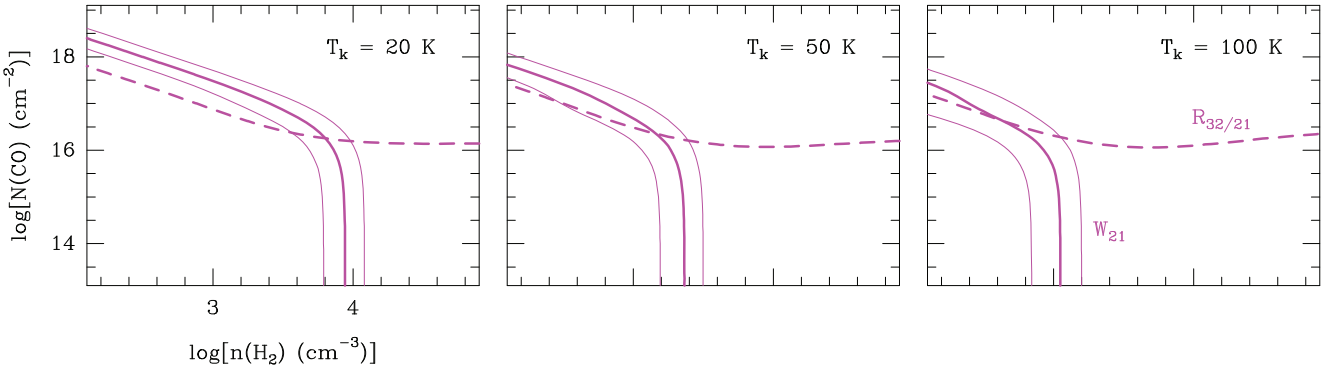


Figure 8. Results of RADEX fitting for $T_k = 20$ K, $T_k = 50$ K, and $T_k = 100$ K. The dashed contours represent the measured CO (3→2)/(2→1) ratio; the solid contours represent the CO $J = 2 \rightarrow 1$ integrated intensity, with its uncertainties. The intersection of the two sets of contours indicate the range of possible values for $n(H_2)$ and $N(CO)$.

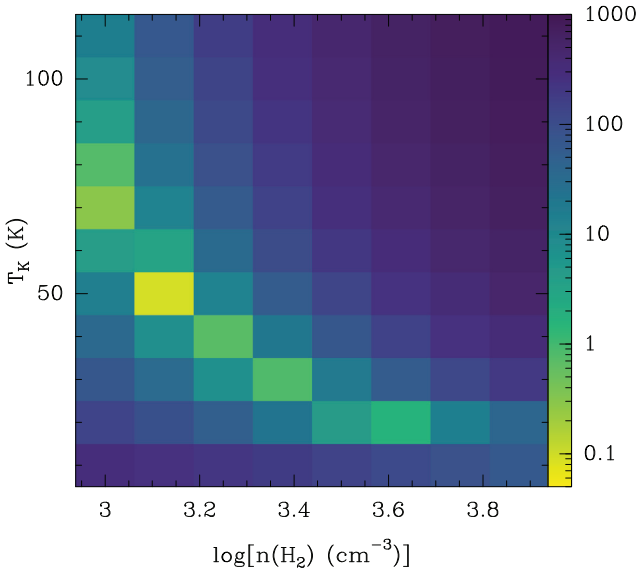


Figure 9. χ^2 surface of the RADEX models, in logarithmic colour scale, as a function of T_k and $n(H_2)$. The models in this plot correspond to the best-fitting $N(CO) = 2.4 \times 10^{16}$ cm^{-2}.

Once we constrained the parameter space, we followed a reduced χ^2 minimization technique to find the model that better reproduces the observed line intensities, such that

$$\chi^2 = \sum_{i=1}^{2} \left(\frac{W_i^{\rm rad} - W_i^{\rm obs}/F_i}{\Delta W_i^{\rm obs}} \right)^2, \quad (4)$$

where W_i is the integrated intensity of the $(i+1) \rightarrow i$ transition and F_i is the corresponding filling factor. Fig. 9 shows the fit χ^2 surface as a function of T_k and $n(H_2)$. We find that the model that best fits the observations is that with $T_k = 50$ K, $N(CO) = 2.4 \times 10^{16}$ cm^{-2}, and $n(H_2) = 1.3 \times 10^3$ cm^{-3}. The solution points to a moderately thick opacity in the emitting medium, with optical depths of $\tau_{21} = 1.2$ and $\tau_{32} = 0.8$ for this temperature range. As a cross-check, we used the derived parameters to predict the ^{13}CO $J = 2 \rightarrow 1$ integrated intensity, for a range of ^{13}CO column densities. The best match is obtained for $N(^{13}CO) = 7.5 \times 10^{14}$ cm^{-2}, which yields an isotopic ratio of ∼30. This value agrees with the $R_{12/13}$ previously discussed.

Finally, we repeated the same procedure to study the excitation conditions of the other components, C1–C3. In this case, as the emission is widespread – in fact, much larger than the beam – we did not apply a correction for beam dilution. We obtained column densities below 10^{16} cm^{-2}, but we were unable to properly constrain the kinetic temperature of the gas. We found many possible solutions, starting from the typical temperatures of a cold cloud, around ∼10 K. All these solutions occurred roughly at constant pressure ($n \times T$), which suggest an equilibrium situation. In addition, the lines were always more optically thin ($\tau < 1$), in contrast with the gas of the ring, which is significantly more opaque. These differences suggest that component C4 is indeed subject to slightly different excitation conditions. LVG results of the four components are compiled in Table 3.

Table 3. LVG results for the four components under analysis. From left to right, kinetic temperature, CO column density, H_2 volume density and optical depth. Values for components C1–C3 are computed for a reference temperature of 30 K.

	T_k (K)	$N(CO)$ (10^{16} cm^{-2})	$n(H_2)$ (10^3 cm^{-3})	τ_{21}	τ_{32}
	20	1.8	5.6	0.8	0.6
Ring (C4)	50	2.4	1.3	1.2	0.8
	100	4.2	1	2.4	1.2
C1	30	0.24	10	0.1	0.2
C2	30	0.75	4.2	0.2	0.2
C3	30	0.18	10	0.1	0.1

4.2.1 *Estimate of the ring mass*

We can use the average CO column density derived with RADEX to provide a crude estimate of the mass of the ring. The total mass of molecular gas is given by

$$M = 2 m_H \, f_{He} \, N(CO) \, X_{CO}^{-1} \, \Omega_{sou} \quad (5)$$

where m_H is the mass of the hydrogen atom, f_{He} is the He correction factor, X_{CO} is the relative [CO/H_2] abundance, and Ω_{sou} is the solid angle subtended by the source. Adopting a cosmic [CO/H_2] abundance of $X_{CO} = 10^{-4}$ and considering that the ring subtends an area of about ∼0.63 pc^2 at $d = 6$ kpc, we obtain a total mass of 2.7 ± 0.9 M$_\odot$, a result comparable with molecular gas masses found in other LBVN: in η Car, the equatorial torus contains 1–5 M$_\odot$ of molecular material (Smith et al. 2018a), and the molecular ring of MN101 has a mass of 0.6 ± 0.1 M$_\odot$ (Bordiu et al. 2019).

It is worth to highlight that this estimate is strongly affected by the determination of the X_{CO} factor and its associated uncertainties. Many

Downloaded from https://academic.oup.com/mnras/article/500/4/5500/5996198 by INAF Trieste (Osservatorio Astronomico di Trieste) user on 20 January 2021

LBVN are deficient in C and O, and consequently underabundant in CO (e.g. η Car, Morris et al. 2017). Should this be the case for AG Car as well, the mass of the ring could be substantially higher.

4.3 Origin of the molecular ring

As shown in previous sections, the ring surrounding AG Car is composed of moderately dense, warm gas slowly expanding into the ISM. The physical connection between the molecular gas and the star, as inferred from morpho-kinematic features and excitation conditions, seems evident. The ring is seen nearly edge-on, with an inclination of $\sim$70°. This is in excellent agreement with the viewing geometry proposed by Groh, Hillier & Damineli (2006) and Groh et al. (2009b), who measured a remarkably high rotation velocity for the star ($v \sin i = 220\,\mathrm{km\,s^{-1}}$) and concluded that we necessarily see AG Car from the equator. Considering this, we can safely assume that the ring lies in – or at least close to – the equatorial plane of the star. Such an assumption is further supported by the orientation of optical continuum jet found by Nota et al. (1992), which should be relatively aligned with the rotation axis of AG Car. Fig. 10 shows the ESO Faint Object Spectrograph and Camera (EFOSC) optical continuum image of AG Car, with the CO contours superimposed. The ring and the jet appear perfectly perpendicular in projection, with P.A. of 135° and 225°, respectively. However, an equatorial ring may be the result of very different physical processes. Below, we discuss possible formation scenarios and their implications.

4.3.1 Swept-up pre-existing material

One possibility is that CO traces a remnant of the parent molecular cloud in which the star formed, which has been compressed by the action of the stellar wind. However, this interpretation involves some problems, as massive stars like AG Car sustain very fast winds of $\sim$1000 km s^{-1} in the main sequence. For several Myrs, these winds sweep up the stellar neighbourhood, eroding and even completely destroying the natal clouds and carving humongous cavities in the ISM. These so-called wind-blown bubbles have scales much larger than the size of ring, even spanning several tens of pc (Garcia-Segura, Mac Low & Langer 1996). Should the CO arise from compressed ISM material, one would expect to find it farther from the star, towards the edges of a wind-blown bubble. *Herschel* images revealed that AG Car is in fact immersed within a cavity about 5 arcmin ($\sim$9 pc) in diameter, where material has been mostly evacuated (see fig. 3 in VN15).

Even so, as Nota et al. (2002) pointed out, aspherical winds due to stellar rotation could result in slower velocities near the equatorial plane of the star, thus 'protecting' ISM material at low latitudes. Yet, the long-term survival of a compact structure so close to the star is mainly determined by the wind density: a fast but not very dense stellar wind would struggle to evacuate the densest parts of a molecular cloud. The dynamical age of the ring, however, favours a more recent, post-main-sequence origin, not more than $\sim 10^5$ yr ago.

4.3.2 A binary interaction remnant

As a second formation hypothesis, one may invoke a binary scenario. The possible binary nature of AG Car has been long discussed in literature ever since the discovery of its bipolar nebula, and particularly, its helical jet, which strongly suggests some kind of precession (Paresce & Nota 1989; Nota et al. 1992).

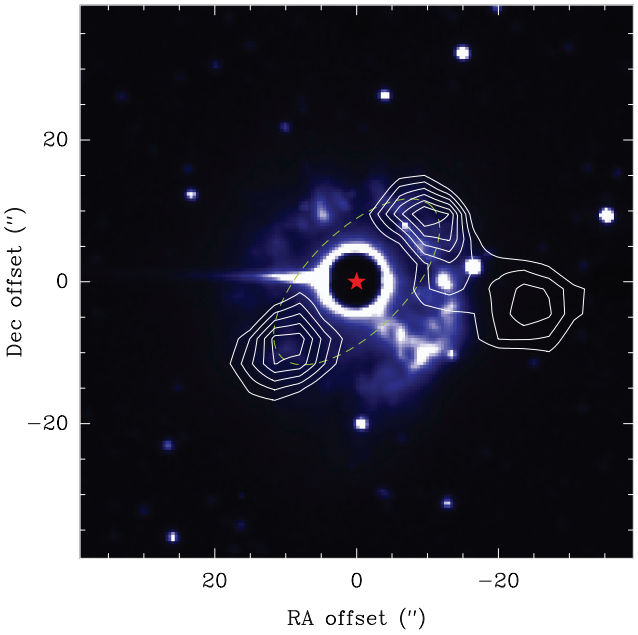


Figure 10. Relative orientation of the optical jet and the molecular ring. EFOSC1 coronographic continuum image of AG Car and its nebula in colour scale (Vamvatira-Nakou et al. 2015). ACA+TP CO $J = 2 \rightarrow 1$ intensity map superimposed as contours. Contours start at 50 per cent of the peak intensity, showing only the ring blobs, for the sake of clarity. The dashed ellipse is displayed to highlight the extent of the structure. The red marker indicates the position of the star. The bright spike to the east is an imaging artefact.

In recent times, the traditional view of LBV stars in the frame of single-star evolution has been challenged. The apparent isolation of most LBVs from OB associations, their phenomenological heterogeneity as a class, and their role as potential SN progenitors, have led some authors to propose an alternative evolutionary paradigm, in which LBVs likely arise from binary interaction. Under this novel framework, two possible formation pathways are considered: either LBVs are *rejuvenated* mass gainers in close binary systems, which end up kicked out by their companion's SN; or they are produced following a binary merger event (Justham, Podsiadlowski & Vink 2014; Smith & Tombleson 2015; Smith 2016; Aghakhanloo et al. 2017).

Assuming that AG Car is part of a close interacting binary, a non-conservative Roche Lobe overflow (RLOF) episode would result in a mass leakage through the outer Lagrange point of the system (L2). This leakage would effectively create a ring-like structure, slowly expanding outwards. Besides, the gainer not only accretes mass in the process, but also angular momentum, speeding up its rotation, which would be consistent with the enhanced rotation of AG Car. This kind of non-conservative mass-transfer interaction has been previously suggested as the driving mechanism in other non-LBV sources that exhibit equatorial ring-like structures, such as the less massive binary RY Scuti (Smith et al. 2011) or SBW1, a very luminous, 18–25 $M_\odot$ BSG (Smith, Bally & Walawender 2007). Still, any assumptions on the binarity of AG Car are highly speculative and must be regarded with caution. So far, the search for a companion has been unfruitful, yielding negative results even at X-ray wavelengths (Nazé, Rauw & Hutsemékers 2012). However, spectroscopic signatures of potential companions may be hidden by the rotationally broadened lines of AG Car. In any case, binarity does not seem to be an extremely common feature among the LBV family, with only a handful of them being

Downloaded from https://academic.oup.com/mnras/article/500/4/5500/5996198 by INAF Trieste (Osservatorio Astronomico di Trieste) user on 20 January 2021

present-day binaries, such as η Car (Damineli et al. 2000) and HR Car (Boffin et al. 2016).

On the other hand, the binary merger hypothesis allows us to circumvent the lack of observational evidence for a companion of AG Car. The merger mechanism described by Justham et al. (2014) depicts a massive binary in which the primary, expanding as it evolves beyond the main-sequence, fills its Roche lobe transferring mass on to the secondary. For certain mass ratios, the system enters a contact phase due to expansion of the secondary's envelope. Eventually, the system destabilizes and a merger occurs. This mechanism could also lead to the formation of rings, as equatorial mass outflows are expected during the merging process as a consequence of the common envelope rotation. The merger idea, which was already introduced two decades ago for some B[e] stars (Langer & Heger 1998; Pasquali et al. 2000), has recently become one of the preferred explanations for η Car's Great Eruption in the 1840s. The outburst would have been triggered by a merger within a hierarchical triple system, leading to the current LBV + O/WN binary (Portegies Zwart & van den Heuvel 2016; Smith et al. 2018b; Toonen et al. 2020) and giving rise to an equatorial torus. While it is difficult to infer whether AG Car has undergone a similar process, we note that many of its features (bipolarity, enhanced rotation, He and N abundances) are predicted for the BSG/LBV products of massive binary mergers, making this hypothesis a fascinating possibility worth to be further explored.

In the general picture, the portrait of LBVs as products of binary interaction seems able to explain many of their peculiarities. The formation of the slowly expanding triple ring system in SN1987A has been equally linked to a possible binary merger (Morris & Podsiadlowski 2007), promoting binarity and rotation as two key ingredients of the sometimes elusive connection between LBVs and supernovae.

4.3.3 An equatorially enhanced outflow

Finally, another possible explanation sticking to the traditional single-star scenario is that the molecular ring in AG Car originated from an equatorially enhanced mass-loss episode. This kind of non-spherical mass-loss seems to be a common phenomenon in LBV stars, as many of them are surrounded by dusty or gaseous equatorial tori, such as η Car (Morris et al. 1999; Smith et al. 2018a), HD168625 (O'Hara et al. 2003), and MN101 (Bordiu et al. 2019). However, little is known about the mechanisms behind the formation of discs or ring-like structures around single massive stars.

Stellar rotation is thought to play a crucial role in the shaping of stellar winds throughout the different evolutionary stages of massive stars. In this context, we may explain the formation of a gaseous ring in AG Car by invoking a rotationally induced bistability mechanism. The bistability jump would produce increased mass fluxes and slower winds at low latitudes near the stellar equator, as a direct outcome of the decrease in the effective gravity $g_{\rm eff}$ and the subsequent gravity darkening (Lamers & Pauldrach 1991; Pelupessy, Lamers & Vink 2000). Similarly, at higher latitudes, the winds would be faster but less dense.

By virtue of this mechanism, aspherical winds and equatorially enhanced mass-loss are strongly favoured in fast-rotating stars with high radiation pressures (Maeder & Desjacques 2001). AG Car, which rotates at a significant fraction of its break-up velocity at least during its hottest phase (up to 86 per cent, Groh et al. 2006), satisfies these two conditions. Leitherer et al. (1994) found two independent pieces of evidence that support this scenario: (1) a significant – and variable – degree of polarization in AG Car, interpreted as an equatorial density enhancement of the stellar wind, and (2), a two-component wind structure: a slow and dense wind, traced by recombination lines, in coexistence with a faster and less dense component, seen in ultraviolet absorption lines.

Another important issue to address is the survival of molecular gas in the proximity of AG Car. For molecules to form out of the stellar wind, a certain degree of shielding against the strong far-ultraviolet radiation must be provided. In this regard, AG Car may somehow be an analog of B[e] supergiants, where slowly expanding, rotating discs or rings of neutral material have been observed. The formation mechanism of such structures has been tentatively linked to nearly critical stellar rotation as well (Zickgraf et al. 1986; Oudmaijer et al. 1998; Curé, Rial & Cidale 2005; Kraus 2006; Kraus, Borges Fernandes & de Araújo 2010). The equatorial winds of B[e]SGs provide the adequate conditions, in terms of temperature and density, for the formation and survival of significant amounts of dust and molecules (Liermann et al. 2010), but B[e]SG discs are much smaller, spanning only a few hundreds of au. In the case of AG Car, the expansion of the wind over large scales would involve an important decrease in density. Perhaps, an inhomogeneous stellar wind – which is a common feature in many hot, massive stars, see e.g. Contreras, Montes & Wilkin (2004) – would make possible the formation of molecules within denser clumps, that would provide the necessary protection against ionizing photons. Interestingly, modelling of the nebular dust content by Voors et al. (2000) predicts a population of very large grains (with sizes up to 40 μm), which are typically found in circumstellar discs. If such a disc exists in AG Car, it would effectively shield the gas, favouring the formation of molecules in its cold outskirts.

Our estimate of the dynamical age of the ring is slightly high compared to the characteristic time-scales of the LBV phase, a few 10^3–10^4 yr. Thus, the structure may have formed in a pre-LBV stage. Along this line of reasoning, some authors have proposed that the main nebula of AG Car was expelled before reaching the LBV phase. Smith et al. (1997), Voors et al. (2000), and Lamers et al. (2001) found nebular abundances of N and O different from the values expected for CNO-enriched material, suggesting that the nebula is composed of 'mildly processed' matter, still far from CNO-equilibrium and thus consistent with older ejecta from a previous BSG or RSG phase. These findings, although not entirely conclusive, might also explain the relatively high $R_{12/13}$ that we measure, more compatible with a moderate degree of processing.

Likewise, the low expansion velocity of the ring is another interesting issue. If we work under the hypothesis that the ejection took place in a pre-LBV stage, a $v_{\rm exp}$ of 3.5 km s^{-1} is in agreement with the typical velocities of RSG winds, of 5–10 km s^{-1}. The possible occurrence of an RSG phase in AG Car, however, needs to be investigated, in view of the apparent lack of very luminous RSGs in the HR diagram (the so-called 'red-supergiant problem', Walmswell & Eldridge 2012). On the other hand, BSG winds are faster and more compatible with the expansion velocity of $\sim$70 km s^{-1} measured in the main nebula. This probably indicates that the ring originated in a separate episode of mass-loss, which may have been relatively steady, in contrast with the main nebula, related to a more eruptive event. Never the less, the measured expansion velocity only reflects the current situation, but the wind may have been faster in the past, resulting in a younger structure as discussed in Section 4.1. In such case, depending on the age, we may obtain time-scales consistent with an ejection event during the LBV phase, which would require further explanations for the observed chemistry.

Downloaded from https://academic.oup.com/mnras/article/500/4/5500/5996198 by INAF Trieste (Osservatorio Astronomico di Trieste) user on 20 January 2021

Table 4. Model parameterization. Rotation velocities, v_ϕ, refer to the inner radius of the ring.

Model	Velocity law	Parameters
1	Rotation	$v_\phi = 1\,\mathrm{km\,s^{-1}}$
2	Expansion	$v_{\rm exp} = 3.5\,\mathrm{km\,s^{-1}}$
3	Expansion + rotation	$v_\phi = 1\,\mathrm{km\,s^{-1}}$, $v_{\rm exp} = 3.5\,\mathrm{km\,s^{-1}}$
4	Expansion + turbulence	$v_{\rm exp} = 3.5\,\mathrm{km\,s^{-1}}$, $v_{\rm turb} = 0.25\,\mathrm{km\,s^{-1}}$

4.4 A closer view to CO kinematics

We have built a simple model to better understand the kinematics of the ring, and also to cross-check the validity of the RADEX fit. To do so, we used LIME (Brinch & Hogerheijde 2010), a 3D non-LTE code that solves radiative transfer by simulating ballistic photon propagation through unstructured Delaunay grids, calculating level populations and predicting the resulting spectra for a given transition, according to the LAMDA data base collisional coefficients (Schöier et al. 2005).

Due to the modest spatial and spectral resolution of our data, we made several assumptions to keep the model as simple as possible; we supposed an axisymmetric ring located at 6 kpc and described by power-law density and temperature profiles of the form r^{-2}. To avoid overinterpreting our maps, instead of fitting the observed data, we qualitatively compared the overall morpho-kinematic features in the structure with those obtained with different kinematic models. Therefore, we adopted the density and temperature outputs of RADEX as reference values for the power-law profiles. Regarding the geometrical parameters, we adopted an inner radius of 0.3 pc, a half opening angle of 10°, an inclination of 70° and a position angle of 135° east of north.

We created four models to explore different possibilities for the velocity structure of the gas, namely: a purely rotating ring with differential rotation (model 1); a radially expanding ring with an outflow velocity of $3.5\,\mathrm{km\,s^{-1}}$ (model 2); an expanding ring with a differential rotation component (model 3); and an expanding ring with macro-turbulence, i.e. with random departures from the expansion velocity law, of up to $0.25\,\mathrm{km\,s^{-1}}$ (model 4). Model parameters are compiled in Table 4. For each of the models, LIME produced a synthetic CO $J = 2 \rightarrow 1$ cube, which was later convolved to the ACA beam and re-gridded to allow for a direct comparison with the original data.

Fig. 11 compares the four models as channel maps in the velocity range of interest. Not surprisingly, the rotating ring (model 1) fails to reproduce the shape and velocity extent of the ring, with all the emission significantly concentrated around the systemic velocity. The other three models are able to reproduce both the extent of the ring and the overall clockwise pattern satisfactorily. Still, we note that the arc-like features that connect the lobes at intermediate velocities (from 29.5 to 30.77 and 34.58 to 35.85 $\mathrm{km\,s^{-1}}$) can only be reproduced by models 3 and 4, i.e. if we add rotation or turbulence to the expanding ring. None of the models reproduce the asymmetric spatial distribution between 32 and $33.3\,\mathrm{km\,s^{-1}}$ correctly. Ring inhomogeneities or clumpiness, not considered here, may account for the observed differences.

Models 3 and 4 also reflect the overall morphology of the integrated intensity map from 29 to 36 $\mathrm{km\,s^{-1}}$ (e.g. Fig. 12 for model 3). Indeed, we found the integrated fluxes to be consistent within a $\sim$ 10 per cent, thus confirming that the average values for density and temperature obtained with RADEX are able to reproduce the observed intensities.

While the presence of turbulent motions in the wind of an unstable star is somewhat expected, the physical feasibility of the expanding–rotating ring model deserves a comment. In principle, any material expelled from the stellar surface, whatever the mechanism for triggering the ejection, will tend to move radially in the long term. In the case of a fast-rotator like AG Car, the ejecta could be initially lifted with a non-negligible rotational component to preserve angular momentum. However, this component will progressively fade as the ring dissipates radially and interacts with the surrounding medium. Moreover, to keep a stable rotation, the material needs to be either gravitationally or magnetically bound to the star. These mechanisms, though, operate only at short distances, but the molecular ring of AG Car is $<10^5$ yr old and far away from the star. Consequently, if the gas actually rotates as indicated by model 3, there should be another mechanism at work responsible for that rotation. Further observations at higher velocity resolution will allow for a better understanding of the gas dynamics.

5 MASS-LOSS HISTORY OF AG CAR

The different evolutionary stages of AG Car have left a footprint in its environment, shaping its circumstellar medium (CSM) in complex manners due to variable stellar winds and episodic mass eruptions. The detection of a molecular ring surrounding the star provides additional information about its recent mass-loss history. It is therefore important to understand how this molecular gas relates to the other components in the CSM.

Broadly speaking, the CSM around AG Car can be described in terms of two independent nebular structures: a detached dusty shell, bright in the infrared; and an ionized nebula, clearly visible in optical and radio continuum images. These structures present strong morpho-kinematic hints of bipolarity. Across the NE–SW direction, two symmetric bright clumps at position angle $\sim$35° and $\sim$225° are evident. In addition, the measured expansion velocity of the shell increases notably (by about $20\,\mathrm{km\,s^{-1}}$) along this direction (Nota et al. 1992). Both the orientation of the clumps and the velocity increase are signposts of a bipolar mass outflow, in which case the bright clumps would correspond to gas density enhancements in the polar 'caps' of the structure, where more material is being accumulated. Fig. 13 shows the location of the CO gas with respect to the dust and the ionized structures. Although an accurate spatial comparison is not possible given the limited resolution of the molecular data, we note that, while the dust and the ionized gas are mostly co-spatial, the molecular gas seems to be complementary: the most intense CO clumps are found along the SE–NW axis, i.e. the direction of the slight elongation of the nebula (Voors et al. 2000).

The molecular ring somewhat constrains the overall geometry of the CSM: an inhomogeneous, nearly spherical expanding shell, disrupted by a slightly faster bipolar outflow and enclosed by an equatorial density enhancement. What is clear, though, is that the equatorial density enhancement should be older than the shell, since the two structures have comparable scales but very different expansion velocities. This geometry, coherent from an evolutionary perspective, can be explained attending to the standard wind-interaction model, which has been proposed to explain the morphologies of other LBVN with aspherical symmetries (e.g. Frank, Balick & Davidson 1995). In this particular scenario, we can imagine AG Car suffering an equatorial mass-loss enhancement, in the form of a dense, steady wind, some $\sim 10^5$ yr ago. This wind would slowly expand into the ISM, sweeping any remaining ambient material. At some point, the wind would get colder and form molecules. A few $\sim 10^4$ yr later, a faster isotropic outflow may take place. This new wind would eventually reach the slower, previous one, interacting with a torus-like density distribution. The result of such interaction is the

Downloaded from https://academic.oup.com/mnras/article/500/4/5500/5996198 by INAF Trieste (Osservatorio Astronomico di Trieste) user on 20 January 2021

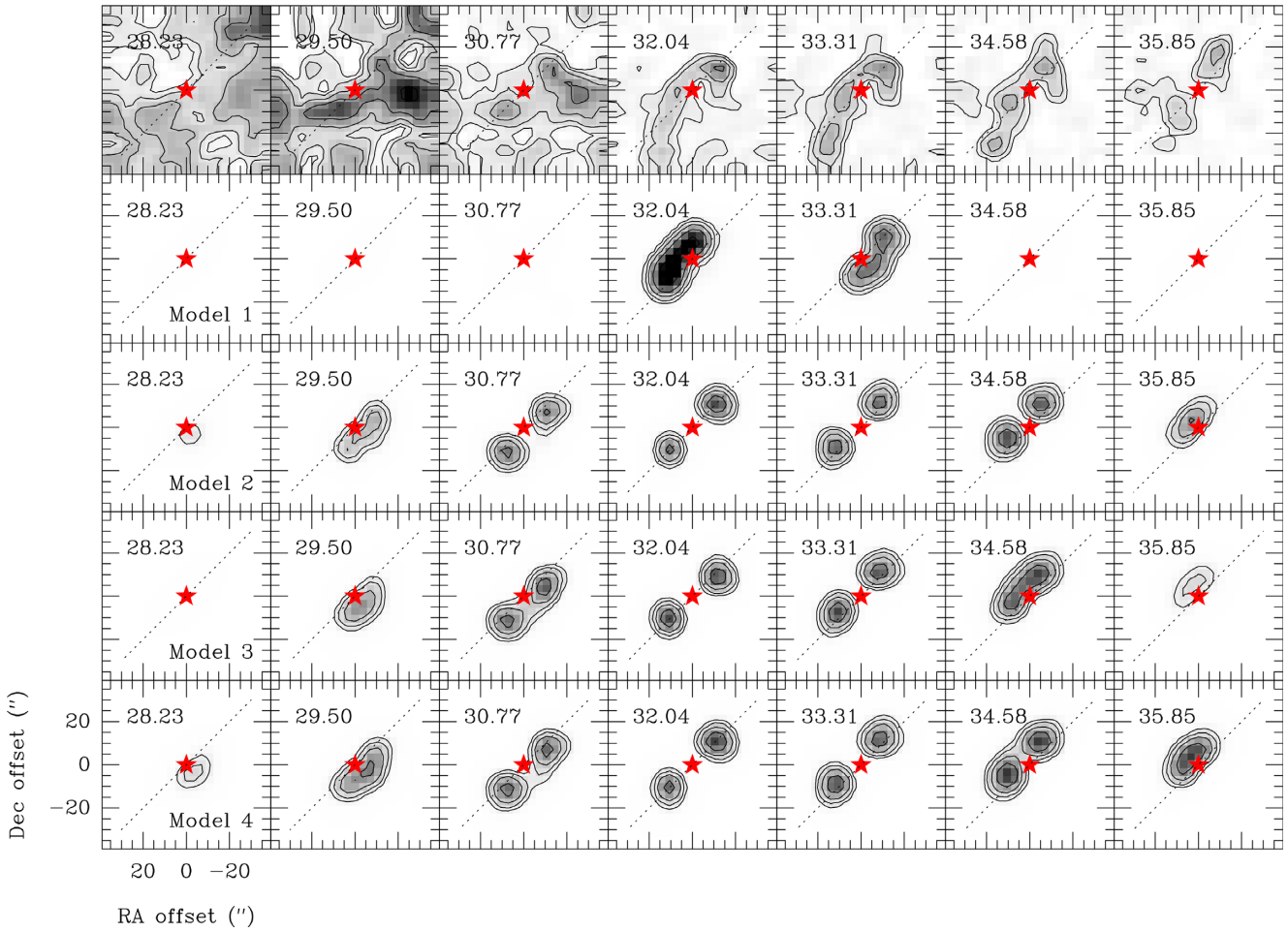


Figure 11. Comparisons of the observed CO $J = 2 \rightarrow 1$ channel maps (top row) with different kinematic models: a rotating ring, a purely expanding ring, a expanding ring with rotation, and an expanding ring with macroturbulence. All the maps share the same intensity scale. Contours at 0.5, 1, 2, 4, and 8 K. The red marker indicates the position of the star and the dashed line represents the direction of the major axis of the structure. The LSR velocity is displayed in the top left corner of each panel.

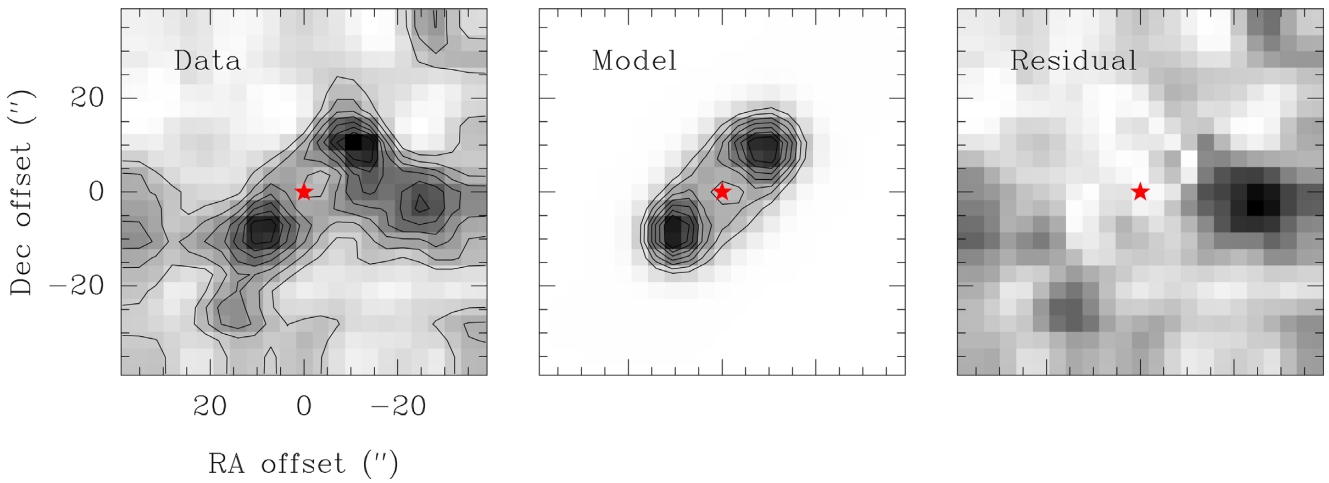


Figure 12. Comparison of the observed CO $J = 2 \rightarrow 1$ intensity map with that of model 3. The residual map is shown for reference. The red marker indicates the position of the star.

formation of a bipolar nebula. The final shape – i.e. the degree of bipolarity – is modulated by several factors, including the rotation velocity of the star (Maeder & Desjacques 2001), and may range from an ellipsoid to a peanut-like structure. The most extreme case of such interaction is, of course, η Car and the Homunculus Nebula. In this sense, VN15 suggest that the ejection of the shell took place in a period of slow rotation, which is consistent with the moderate degree of bipolarity observed.

Downloaded from https://academic.oup.com/mnras/article/500/4/5500/5996198 by INAF Trieste (Osservatorio Astronomico di Trieste) user on 20 January 2021

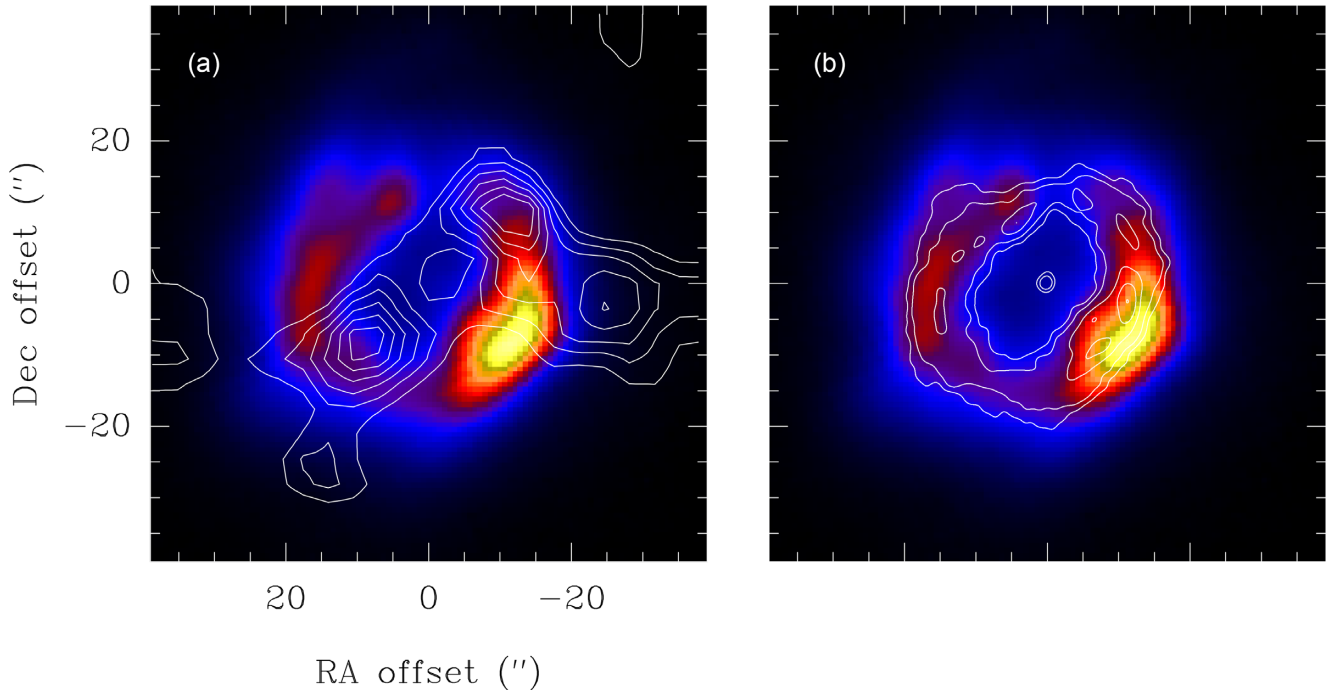


Figure 13. Multiwavelength comparison of the nebular material around AG Car. (a) *Herschel* PACS 70 μm image in colour scale with the ACA CO $J = 2 \rightarrow 1$ contours superimposed. The levels are the same as in Fig. 3(b). The same as (a) but with the ATCA radio continuum contours at 5.5 GHz (Duncan & White 2002).

VN15 estimated a total mass of ionized gas of $6.6 \pm 1.9\,M_\odot$, from the Hα and radio continuum fluxes. Similarly, they derived a dust mass of $0.20 \pm 0.05\,M_\odot$ from the SED modelling. Using our continuum data and following their approach, we obtain a nebular ionized mass of $3.9 \pm 1.9\,M_\odot$, smaller but still in agreement within uncertainties with VN15's estimate. However, as noted in Section 3.2.2, we may be missing some flux with ACA. The total combined mass of ionized and molecular gas thus adds up to $9.3 \pm 2.8\,M_\odot$ (or $5.9 \pm 2.8\,M_\odot$ if we take our estimate). This agrees again, within uncertainties, with the value proposed by VN15 ($15 \pm 4.5\,M_\odot$), who adopted a gas-to-dust ratio of ∼40 to estimate the contribution of neutral gas. This means that, assuming a stellar origin, the molecular gas around AG Car traces at least a ∼ 30 per cent of the mass lost by the star.

The gas and dust masses can be translated into mass-loss rates by estimating the kinematic duration of the events that produced the observed structures. This can be done by computing the temporal difference between the inner and outer shell radius for a constant expansion velocity. Following this method, VN15 derived a kinematic duration of 1.1×10^4 yr for the mass-loss episode that created the infrared nebula, taking an inner and outer radii of 0.4 and 1.2 pc, respectively. It is a useful exercise to do the same and provides a crude estimate of duration of the molecular outflow. However, we warn that the reliability of this method is limited, in the sense that the emitting region may be smaller than the beam therefore we decided to conservatively adopt the size of the ACA beam, of about 7 arcsec, as the reference 'width' of the ring. In addition, we work under the assumption that the expansion velocity does not change and there is no velocity dispersion across the ring, which is probably unrealistic. For $v_{\rm exp} = 3.5\,{\rm km\,s^{-1}}$, we obtain an approximate duration of 5.6×10^4 yr. This is just a loose upper limit, but still, it is interesting to realize that it is about five times larger that the duration of VN15 for the isotropic mass-loss episode. This probably suggests that the equatorial enhancement was more steady and less eruptive, which is, again, in line with the proposed formation scenario.

The average mass-loss rate that produced the molecular ring is thus $\dot{M} = (4.8 \pm 1.6) \times 10^{-5}\,M_\odot\ {\rm yr^{-1}}$, but it could be substantially higher if the structure is more compact than the ACA beam. We can compare this value with the current mass-loss rate. Under the assumption that the flux density of the point-like source measured at 225 GHz is due to stellar wind, we can approximate the current mass-loss rate of AG Car using the empirical formula by Panagia & Felli (1975) for expanding envelopes around hot stars, in which we assume full ionization and standard cosmic abundances, so that

$$\dot{M} = 6.7 \times 10^{-4} v_\infty F_\nu^{3/4} d^{3/2} (\nu \times g_{\rm ff})^{-0.5}, \quad (6)$$

where v_∞ is the terminal wind velocity in ${\rm km\,s^{-1}}$, d is the distance in kpc, F_ν is the measured flux in mJy, and ν is the central frequency in Hz. $g_{\rm ff}$ is the free–free Gaunt factor, which we approximate as $g_{\rm ff} = 9.77(1 + 0.13 \log \frac{T^{3/2}}{\nu})$, where T is the wind plasma temperature (Leitherer & Robert 1991). Providing a single value for the terminal wind velocity of AG Car is tricky. Long-term spectroscopic monitoring by Stahl et al. (2001) between 1989 and 1999 revealed abrupt changes from 225 to 30 ${\rm km\,s^{-1}}$. The wind also changes drastically between consecutive visual minima, with values of 300 ${\rm km\,s^{-1}}$ between 1985 and 1990 and 105 ${\rm km\,s^{-1}}$ in 2000–2001. Therefore, since we are now on the way to a new visual maximum, we adopt a conservative value of 100 ${\rm km\,s^{-1}}$, compatible with the wind velocity measured near the 1995 maximum. For a wind temperature of 10^4 K and a distance of 6 kpc, we obtain a mass-loss rate of $\dot{M} = (1.55 \pm 0.21) \times 10^{-5}\,M_\odot\ {\rm yr^{-1}}$. This mass-loss rate is in very good agreement with Groh et al. (2009a) estimates of the quiescent $\dot{M}$ of AG Car, of $1.5 \times 10^{-5}\,M_\odot\ {\rm yr^{-1}}$.

Downloaded from https://academic.oup.com/mnras/article/500/4/5500/5996198 by INAF Trieste (Osservatorio Astronomico di Trieste) user on 20 January 2021

6 CONCLUSIONS

We present APEX single-dish and ALMA/ACA interferometric observations of CO, ^{13}CO, and continuum towards AG Car, confirming the existence of a molecular structure associated with this LBV star. Below, we summarize the key findings in this work:

(i) By means of CO and ^{13}CO ALMA/ACA data, we report the detection of a molecular ring-like structure around AG Car, confirming the hypothesis by Nota et al. (2002). The morpho-kinematic features of the structure can be explained by a slowly expanding ring or torus.

(ii) We model the excitation conditions of the gas under non-LTE conditions. We used the available CO and ^{13}CO $J = 2 \rightarrow 1$ and CO $J = 3 \rightarrow 2$ single-dish data to provide average estimates for the whole ring. The gas in the structure is warm, with a kinetic temperature of about 50 K, not very dense, with H_2 densities of a few 10^3 cm^{-3}, and moderately thick. The total mass of molecular gas in the ring is 2.7 ± 0.9 M$_\odot$, subject to uncertainties in the determination of the [CO/H_2] relative abundance. This accounts for at least a ~ 30 per cent of the mass expelled by the star.

(iii) We develop a simple kinematic model to better study gas dynamics, showing that some deviations from pure radial expansion are required to properly reproduce some of the morpho-kinematic features observed in the data, such as (1) the addition of a turbulent component or (2) the superposition of a differential rotational field.

(iv) To explain the presence of a ring-like structure of molecular gas around AG Car, we discuss a number of possible formation scenarios, namely (1) the compression of a remnant of the parent molecular cloud, (2) a RLOF mass transfer episode or a merger event in a close binary, or (3) an equatorial mass outflow. We regard the mass outflow as the most promising, taking into account the evolutionary stage of the star and the evidence available.

(v) We put together a global view of the mass-loss record of AG Car, proposing an overall morphology that integrates dust, ionized, and neutral gas into a physically feasible, unified picture. We also derive a lower limit of the average mass-loss rate of the ring and compare it with the current mass-loss rate of the star derived from the ACA continuum.

The detection of a molecular ring around AG Car adds the missing piece to the mass-loss history of this intriguing source. This work shows that molecules may trace a significant amount of the total mass lost by an evolved massive star. This has important implications for stellar evolution models, which sometimes struggle to properly reproduce the evolution between O/B and Wolf–Rayet stars, in part due to inaccurate mass-loss rate estimates.

Moreover, the results in this paper pave the way for further exploration of AG Car and its complex CSM. To confirm the origin of the ring, explain its survival, and better understand its kinematics, observations at higher angular and velocity resolution are necessary. Looking for other molecules, such as photodissociation region tracers, would also be extremely useful to obtain a more complete chemical characterization of the star. Finally, deeper radio continuum observations would provide valuable hints about the nebular excitation mechanisms and their dependence on the S-Dor cycles. AG Car is, undoubtedly, a unique object, and as such it represents an outstanding chance to learn about the nature of LBV phase and its associated mass-loss phenomena.

ACKNOWLEDGEMENTS

We thank the anonymous referee for comments and suggestions that improved the quality of this paper. We are sincerely grateful to Dr. Damien Hutsemékers for kindly providing the Hα+[N II] and optical continuum EFOSC images of AG Car. This publication is based on data acquired with the Atacama Pathfinder Experiment (APEX). APEX is a collaboration between the Max-Planck-Institut fur Radioastronomie, the European Southern Observatory, and the Onsala Space Observatory. This paper has used the following ALMA data: ADS/JAO.ALMA#2019.1.01056.S. ALMA is a partnership of ESO (representing its member states), NSF (USA), and NINS (Japan), together with NRC (Canada), MOST, and ASIAA (Taiwan), and KASI (Republic of Korea), in cooperation with the Republic of Chile. The Joint ALMA Observatory is operated by ESO, AUI/NRAO, and NAOJ. JRR acknowledges support from projects ESP2017-86582-C4-1-R and PID2019-105552RB-C41 from the Ministerio de Ciencia e Innovación (Spain).

DATA AVAILABILITY

The derived data products generated in this research will be shared on reasonable request to the corresponding author.

REFERENCES

Aghakhanloo M., Murphy J. W., Smith N., Hložek R., 2017, MNRAS, 472, 591
Agliozzo C., Noriega-Crespo A., Umana G., Flagey N., Buemi C., Ingallinera A., Trigilio C., Leto P., 2014, MNRAS, 440, 1391
Boffin H. M. J. et al., 2016, A&A, 593, A90
Bonato M. et al., 2018, MNRAS, 478, 1512
Bordiu C., Rizzo J. R., 2019, MNRAS, 490, 1570
Bordiu C., Rizzo J. R., Ritacco A., 2019, MNRAS, 482, 1651
Brinch C., Hogerheijde M. R., 2010, A&A, 523, A25
Buemi C. S. et al., 2017, MNRAS, 465, 4147
Cerrigone L., Umana G., Buemi C. S., Hora J. L., Trigilio C., Leto P., Hart A., 2014, A&A, 562, A93
Cohen R. S., Grabelsky D. A., May J., Bronfman L., Alvarez H., Thaddeus P., 1985, ApJ, 290, L15
Contreras M. E., Montes G., Wilkin F. P., 2004, Rev. Mex. Astron. Astrofis., 40, 53
Curé M., Rial D. F., Cidale L., 2005, A&A, 437, 929
Damineli A., Kaufer A., Wolf B., Stahl O., Lopes D. F., de Araújo F. X., 2000, ApJ, 528, L101
Dumke M., Mac-Auliffe F., 2010, in Silva D. R., Peck A. B., Soifer B. T., eds, Proc. SPIE Conf. Ser. Vol. 7737, Observatory Operations: Strategies, Processes, and Systems III. SPIE, Bellingham, p. 385
Duncan R. A., White S. M., 2002, MNRAS, 330, 63
Frank A., Balick B., Davidson K., 1995, ApJ, 441, L77
Gaia Collaboration, 2016, A&A, 595, A2
Garcia-Segura G., Mac Low M. M., Langer N., 1996, A&A, 305, 229
Grabelsky D. A., Cohen R. S., Bronfman L., Thaddeus P., May J., 1987, ApJ, 315, 122
Groh J. H., Hillier D. J., Damineli A., 2006, ApJ, 638, L33
Groh J. H., Hillier D. J., Damineli A., Whitelock P. A., Marang F., Rossi C., 2009a, ApJ, 698, 1698
Groh J. H. et al., 2009b, ApJ, 705, L25
Groh J. H., Hillier D. J., Damineli A., 2011, ApJ, 736, 46
Gull T. R., Morris P. W., Black J. H., Nielsen K. E., Barlow M. J., Royer P., Swinyard B. M., 2020, MNRAS, 499, 5269
Humphreys R. M., Davidson K., 1994, PASP, 106, 1025
Humphreys R. M., Lamers H. J. G. L. M., Hoekzema N., Cassatella A., 1989, A&A, 218, L17
Justham S., Podsiadlowski P., Vink J. S., 2014, ApJ, 796, 121

Downloaded from https://academic.oup.com/mnras/article/500/4/5500/5996198 by INAF Trieste (Osservatorio Astronomico di Trieste) user on 20 January 2021

Klein B., Hochgürtel S., Krämer I., Bell A., Meyer K., Güsten R., 2012, A&A, 542, L3
Kraus M., 2006, A&A, 456, 151
Kraus M., Borges Fernandes M., de Araújo F. X., 2010, A&A, 517, A30
Lamers H. J. G., Pauldrach A. W. A., 1991, A&A, 244, L5
Lamers H. J. G. L. M., Nota A., Panagia N., Smith L. J., Langer N., 2001, ApJ, 551, 764
Langer N., Heger A., 1998, in Hubert A. M., Jaschek C., eds, B[e] stars, Astrophys. Space Sci. Libr. Vol 233. Kluwer Academic Publishers, Boston, p. 235
Leitherer C., Robert C., 1991, ApJ, 377, 629
Leitherer C. et al., 1994, ApJ, 428, 292
Liermann A., Kraus M., Schnurr O., Fernand es M. B., 2010, MNRAS, 408, L6
Loinard L., Menten K. M., Güsten R., Zapata L. A., Rodríguez L. F., 2012, ApJ, 749, L4
Loinard L., Kamiński T., Serra P., Menten K. M., Zapata L. A., Rodríguez L. F., 2016, ApJ, 833, 48
Maeder A., Desjacques V., 2001, A&A, 372, L9
Mangum J. G., Shirley Y. L., 2015, PASP, 127, 266
Meynet G., Ekström S., Maeder A., 2006, A&A, 447, 623
Morris T., Podsiadlowski P., 2007, Science, 315, 1103
Morris P. W. et al., 1999, Nature, 402, 502
Morris P. W., Gull T. R., Hillier D. J., Barlow M. J., Royer P., Nielsen K., Black J., Swinyard B., 2017, ApJ, 842, 79
Morris P. W. et al., 2020, ApJ, 892, L23
Nazé Y., Rauw G., Hutsemékers D., 2012, A&A, 538, A47
Nota A., Leitherer C., Clampin M., Greenfield P., Golimowski D. A., 1992, ApJ, 398, 621
Nota A., Pasquali A., Marston A. P., Lamers H. J. G. L. M., Clampin M., Schulte-Ladbeck R. E., 2002, AJ, 124, 2920
O'Hara T. B., Meixner M., Speck A. K., Ueta T., Bobrowsky M., 2003, ApJ, 598, 1255
Oudmaijer R. D., Proga D., Drew J. E., de Winter D., 1998, MNRAS, 300, 170
Panagia N., Felli M., 1975, A&A, 39, 1
Paresce F., Nota A., 1989, ApJ, 341, L83
Pasquali A., Nota A., Langer N., Schulte-Ladbeck R. E., Clampin M., 2000, AJ, 119, 1352
Pelupessy I., Lamers H. J. G. L. M., Vink J. S., 2000, A&A, 359, 695
Portegies Zwart S. F., van den Heuvel E. P. J., 2016, MNRAS, 456, 3401
Rathborne J. M., Burton M. G., Brooks K. J., Cohen M., Ashley M. C. B., Storey J. W. V., 2002, MNRAS, 331, 85
Rizzo J. R., 2019, in ALMA2019: Science Results and Cross-Facility Synergies, Zenodo, available at https://zenodo.org/record/3585400#.X9DyaOlKjlw
Rizzo J. R., Arnal E. M., 1998, A&A, 332, 1025
Rizzo J. R., Jiménez-Esteban F. M., Ortiz E., 2008, ApJ, 681, 355
Rizzo J. R., Palau A., Jiménez-Esteban F., Henkel C., 2014, A&A, 564, A21
Schöier F. L., van der Tak F. F. S., van Dishoeck E. F., Black J. H., 2005, A&A, 432, 369
Smith L. J., 1991, in van der Hucht K. A., Hidayat B., eds, Proc. IAU Symp. 143, Wolf-Rayet Stars and Interrelations with Other Massive Stars in Galaxies. Kluwer, Dordrecht, p. 385
Smith L. J., Stroud M. P., Esteban C., Vilchez J. M., 1997, MNRAS, 290, 265
Smith N., 2016, MNRAS, 461, 3353
Smith N., Davidson K., 2001, ApJ, 551, L101
Smith N., Stassun K. G., 2017, AJ, 153, 125
Smith N., Tombleson R., 2015, MNRAS, 447, 598
Smith N., Bally J., Walawender J., 2007, AJ, 134, 846
Smith N., Gehrz R. D., Campbell R., Kassis M., Le Mignant D., Kuluhiwa K., Filippenko A. V., 2011, MNRAS, 418, 1959
Smith N., Ginsburg A., Bally J., 2018a, MNRAS, 474, 4988
Smith N. et al., 2018b, MNRAS, 480, 1466
Smith N., Aghakhanloo M., Murphy J. W., Drout M. R., Stassun K. G., Groh J. H., 2019, MNRAS, 488, 1760
Sobolev V. V., 1960, Moving Envelopes of Stars. Harvard Univ. Press, Cambridge
Stahl O., Jankovics I., Kovács J., Wolf B., Schmutz W., Kaufer A., Rivinius T., Szeifert T., 2001, A&A, 375, 54
Sterken C., 2003, in American Astronomical Society Meeting Abstracts #202. p. 13.03
Thackeray A. D., 1950, MNRAS, 110, 524
Thackeray A. D., 1977, MNRAS, 180, 95
Toonen S., Portegies Zwart S., Hamers A. S., Band opadhyay D., 2020, A&A, 640, A16
Umana G., Buemi C. S., Trigilio C., Leto P., 2005, A&A, 437, L1
Umana G., Buemi C. S., Trigilio C., Hora J. L., Fazio G. G., Leto P., 2009, ApJ, 694, 697
Umana G., Buemi C. S., Trigilio C., Leto P., Hora J. L., 2010, ApJ, 718, 1036
Vamvatira-Nakou C., Hutsemékers D., Royer P., Cox N. L. J., Nazé Y., Rauw G., Waelkens C., Groenewegen M. A. T., 2015, A&A, 578, A108
van der Tak F. F. S., Black J. H., Schöier F. L., Jansen D. J., van Dishoeck E. F., 2007, A&A, 468, 627
Vassilev V. et al., 2008, A&A, 490, 1157
Voors R. H. M. et al., 2000, A&A, 356, 501
Walmswell J., Eldridge J., 2012, MNRAS, 419, 2054
Wilson T. L., Matteucci F., 1992, A&AR, 4, 1
Wolf B., Stahl O., 1982, A&A, 112, 111
Wu R., Bron E., Onaka T., Le Petit F., Galliano F., Languignon D., Nakamura T., Okada Y., 2018, A&A, 618, A53
Zickgraf F. J., Wolf B., Stahl O., Leitherer C., Appenzeller I., 1986, A&A, 163, 119

This paper has been typeset from a TEX/LATEX file prepared by the author.

Downloaded from https://academic.oup.com/mnras/article/500/4/5500/5996198 by INAF Trieste (Osservatorio Astronomico di Trieste) user on 20 January 2021